Cell Biomaterials

Article

# Geometrically controlled cardiac microtissues promote vascularization and reduce inflammation *in vitro* and *in vivo*

## Graphical abstract

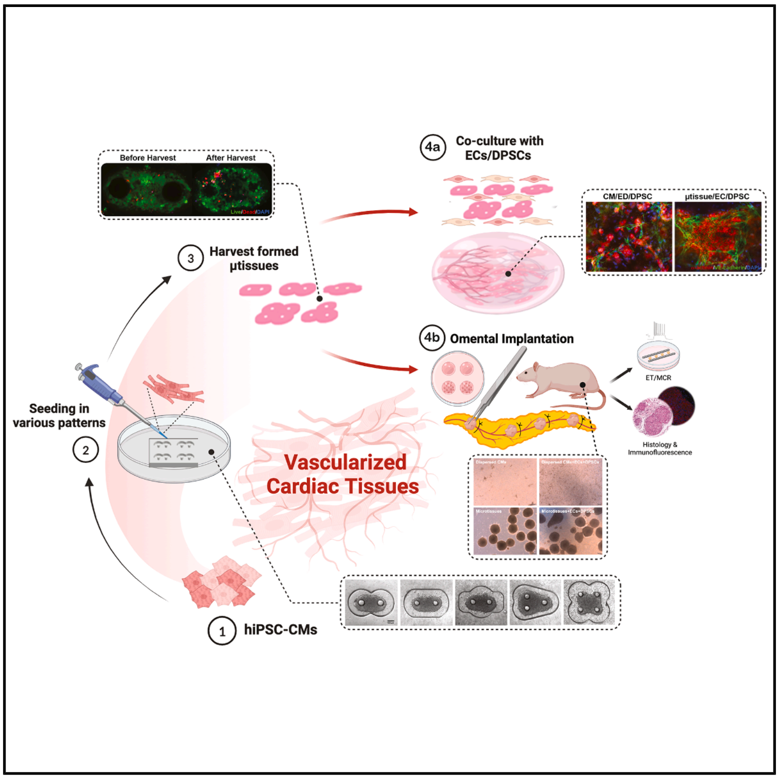

## Highlights

- Anisotropic cardiac microtissues enhance cell alignment and contractility
- Microtissues support vascular integration and reduce inflammation *in vitro*
- *In vivo*, microtissues enhance graft size, vascularization, and reparative macrophages
- Microtissue non-myocytes suppress inflammation via reduced YAP activation

## Authors

Yimu Zhao, Ramak Khosravi,
Krisco Cheung, ..., Ana C. Andreazza,
Gordana Vunjak-Novakovic,
Milica Radisic

## Correspondence

m.radisic@utoronto.ca

## In brief

Geometrically controlled, stem cell-derived cardiac microtissues were evaluated both as vascularized engineered tissues in cell culture and as grafts in the abdominal cavities of nude rats. These engineered microtissues promoted cell alignment for stronger contractions and supported blood vessel formation while minimizing inflammation. Compared with dispersed cells, the microtissues exhibited reduced cell death, lower cellular stress, and balanced signaling for vascular development and inflammatory control. This strategy holds promise for advancing more effective cell-based therapies for heart failure.

Zhao et al., 2025, Cell Biomaterials *1*, 100075
May 27, 2025
https://doi.org/10.1016/j.celbio.2025.100075

Cell Biomaterials

Article

# Geometrically controlled cardiac microtissues promote vascularization and reduce inflammation *in vitro* and *in vivo*

Yimu Zhao,[1,2,3,16] Ramak Khosravi,[2,4,16] Krisco Cheung,[5,16] Karen Shen,[2] Ying Wang,[1,2] Shira Landau,[1,2] Sargol Okhovatian,[1,2] Qinghua Wu,[1,2] Rick Xing Ze Lu,[1,2] Karl T. Wagner,[1,2] David F. Bodenstein,[1,2,8] Sarah A. Shawky,[7] Daniel Vosoughi,[2,8] Erika Leigh Beroncal,[9] Keith Yeager,[10] Carolyn L. Cummins,[7,11,12] Ana C. Andreazza,[9,13,14] Gordana Vunjak-Novakovic,[10] and Milica Radisic[1,2,6,15,17,*]

[1]Institute of Biomedical Engineering, University of Toronto, Toronto, ON M5S 3E3, Canada
[2]Toronto General Hospital Research Institute, University Health Network, Toronto, ON M5G 2C4, Canada
[3]Acceleration Consortium, University of Toronto, Toronto, ON M5S 3E1, Canada
[4]Division of Cardiovascular and Thoracic Surgery, Department of Surgery, Duke University Medical Center, Durham, NC 27710, USA
[5]Department of Bioengineering, University of California, Berkeley-University of California, San Francisco, San Francisco, CA 94720, USA
[6]Department of Chemical Engineering and Applied Chemistry, University of Toronto, Toronto, ON M5S 3E5, Canada
[7]Department of Pharmaceutical Sciences, Leslie Dan Faculty of Pharmacy, University of Toronto, Toronto, ON M5S 3M2, Canada
[8]Institute of Medical Science, University of Toronto, Toronto, ON M5S 3H2, Canada
[9]Department of Pharmacology and Toxicology, University of Toronto, Toronto, ON M5G 2C8, Canada
[10]Department of Biomedical Engineering, Columbia University, New York, NY 10032, USA
[11]Banting and Best Diabetes Centre, Toronto, ON M5G 2C4, Canada
[12]The Heart and Stroke Richard Lewar Centre of Excellence in Cardiovascular Research, Toronto, ON M5S 3H2, Canada
[13]Department of Psychiatry, University of Toronto, Toronto, ON M5T 1R8, Canada
[14]Centre for Addiction and Mental Health, Toronto, ON M5T 1R8, Canada
[15]Terrence Donnelly Centre for Cellular & Biomolecular Research, University of Toronto, Toronto, ON M5S 3E1, Canada
[16]These authors contributed equally
[17]Lead contact
*Correspondence: m.radisic@utoronto.ca
https://doi.org/10.1016/j.celbio.2025.100075

**THE BIGGER PICTURE** For decades, cardiac regenerative medicine has faced a major hurdle: transplanted heart cells fail to survive and integrate, limiting their therapeutic potential. Many attributed this failure to the ischemic environment of damaged heart tissue. However, our study challenges this assumption and shifts the focus to the inherent biological properties of transplanted cells. Using a well-vascularized omentum model to eliminate ischemia as a variable, we found that dispersed induced pluripotent stem cell (iPSC)-derived cardiac cells failed to engraft, disappearing within a week. In contrast, engineered cardiac microtissues—small, structured clusters of heart cells—formed robust, vascularized grafts and triggered a regenerative immune response. The key to this difference lies in the Yes-associated protein (YAP) signaling pathway, which regulates cell survival and inflammation. In dispersed cell transplants, non-myocytes exhibited high YAP activation, leading to inflammatory cytokine secretion and graft failure. However, in microtissues, YAP activation was controlled, supporting cardiomyocyte survival while suppressing inflammation. This study shifts the focus of cardiac regeneration from oxygen supply alone to biophysical and mechanobiological factors that regulate graft survival. By engineering geometrically optimized cardiac microtissues, we can enhance integration, reduce inflammation, and improve graft repair outcomes.

## SUMMARY

Cardiac tissue engineering faces challenges due to inadequate vascularization, poor engraftment, and ineffective strategies to control inflammation. This study explores the benefits of geometrically controlled cardiac microtissues over-dispersed cells. Microtissues derived from human induced pluripotent stem cell-derived cardiomyocytes (hiPSC-CMs) and affixed between two polydimethylsiloxane (PDMS) pillars exhibited cellular alignment and contractile function and were necessary to serve as suitable building blocks for assembling larger tissues. Following implantation into the omentum in nude rats, these tissues exhibited

**robust engraftment, contractility, and vascularization, with significantly reduced inflammation. Compared to dispersed cells, microtissues demonstrated enhanced vessel network formation, reduced cell death (lower lactate dehydrogenase [LDH]), decreased cytotoxicity (lower cell-free mitochondrial DNA [mtDNA]), and decreased Yes-associated protein (YAP) activation in cardiomyocytes and associated non-cardiomyocyte populations. Cytokine analysis revealed elevated pro-angiogenic factors (placenta growth factor [PlGF], endocan, and angiopoietin-2) and reduced inflammatory markers (interleukin-31 receptor A [IL-31 RA], interleukin [IL]-2 R beta, and OX40 ligand) in microtissues compared with dispersed cells, offering a promising approach for cardiac repair and regeneration.**

## INTRODUCTION

Human induced pluripotent stem cell-derived cardiomyocytes (hiPSC-CMs) have emerged as a promising cell source in cardiac tissue engineering. However, their poor post-transplantation survival and limited graft size secondary to ischemia and the host immune response limit their therapeutic potential.[1,2] Increased blood vessel density and perfusion have been shown to improve hiPSC-CMs engraftment and functionality *in vivo*, enhancing their regenerative potential for cell-based therapies; however, these studies rely on pre-formed endothelial networks.[3–5]

To date, many approaches have attempted to incorporate a functional vasculature within cardiac tissues to support grafts that are large enough to support clinically meaningful contractile functions, as in the setting of myocardial infarction (MI) or heart failure.[6] Several publications have demonstrated the pro-angiogenic potential of stromal cells such as dental pulp stem cells (DPSCs), supporting their role in promoting angiogenesis and vasculogenesis[7–9] and leading to their use as supporting cells in engineered tissues.[10,11] Yet, the simple co-culture of CMs with endothelial cells (ECs) and mural cells resulted in premature and segmented lumen structures without sufficient perfusion.[12] A pre-defined, mechanically stable biomaterial-based vasculature within the parenchymal spaces can help, but it confers limited flexibility[13,14] and lacks dynamic remodeling.[13,15,16] Although 3D-printed vascular networks[17–20] can produce complex hierarchical vascular networks within hydrogels, their resolution is typically less than desired and they fail to recapitulate the dynamic crosstalk between capillary endothelium and parenchymal CMs due to the lack of a microvascular network.[21,22]

These challenges are limiting the *in vivo* assembly of large tissues, which are dependent on successful engraftment of transplanted CMs. Furthermore, stable hiPSC-CM engraftment in animal models has previously shown to be dependent on strict immunosuppression regimens, treatment with heat shock therapy, and the addition of complex pro-survival cocktails.[23] Many hiPSC-CM-based interventions stimulate functional cardiac recovery not by local cellular engraftment and differentiation but by a paracrine mechanism that modulates the behavior of surrounding cells.[24] It has proven difficult to establish a clear link between the contractility of transplanted CMs and improvements in host cardiac function.[25] Although low cellular engraftment is typically secondary to the formation of immature, unstable vasculature,[26] one must also take into account the immune properties of the transplanted cells and the inflammatory milieu into which they are introduced.

We hypothesize here that excessive inflammation upon tissue transplantation is another significant contributor to limited graft survival. Modulating the inflammatory properties of engineered tissues and their host environment, along with establishing a perfusable and dynamic vascular network, could therefore promote transplanted cell retention and improve the graft's functional properties.

In this study, we developed a novel approach to address these challenges by generating uniaxially oriented cardiac microtissues, using hiPSC-CMs and cardiac fibroblasts (cFBs) for stromal support (Figure 1), demonstrating that the cardiac microtissues attenuate the inflammatory phenotype in comparison with the dispersed cells, promoting the host endothelial ingrowth to generate functional, vascularized grafts with excellent cellular retention, preserved architecture, and stable functional properties. The microtissue approach presented here may improve cell-based therapies directed at cardiac remuscularization and functional recovery.

## RESULTS

### Micromold geometry and pillar positioning influence microtissue cell alignment

Engineered cardiac tissues require tension for cell elongation, intercellular alignment, and functional maturation.[27] Based on this principle, five pillar-based platforms were designed with different geometries and numbers of pillars (2, 3, and 4) to investigate the effect of pillar arrangement on cellular alignment in microtissues (Figure S1A).

The microwells for tissue generation were approximately 800 μm across the longest axis with 100 μm-diameter pillars. Considering the oxygen diffusion depth of ∼100 μm and the requirement for the low aspect ratio of the pillars required to maintain their integrity after molding, a well depth of 300 μm was selected, similar to the Biowire platform,[28] resulting in an aspect ratio of 3 (Figure S1B). Through a series of adjustments in the fabrication protocol that included modification of spin speed and crosslinking energy (Figures S1C–S1E), a high reproducibility was achieved. Polydimethylsiloxane (PDMS) molds produced from the SU-8 master successfully replicated the features and pillars, as confirmed by bright-field microscopy (Figure S1F). Successful tissue formation was defined as adherence to both pillars and appropriate tissue compaction (Figure S1G).

Vascular microtissues, with networks stable up to 5 days in culture, were first utilized to identify the pattern with optimal tissue formation and the highest success rate, leveraging the

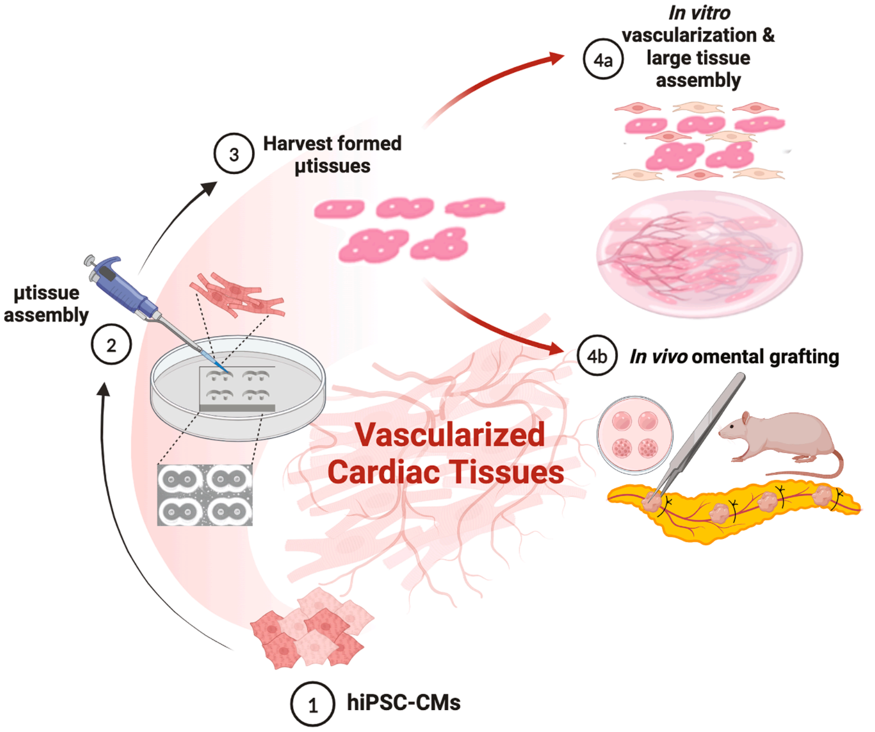

**Figure 1. The microtissue fabrication process and their applications *in vitro* and *in vivo***

hiPSC-CMs were seeded into PDMS molds to generate cardiac microtissues with defined architecture. For *in vitro* applications, these microtissues were combined with endothelial cells (ECs) and dental pulp stem cells (DPSCs) in a fibrin hydrogel to promote vascularization. The approach would be adaptable to facilitate the assembly of larger functional tissues, as well as other *in vitro* downstream applications. Parallel *in vitro* studies involved omental implantation of microtissues in adult athymic nude rats to assess the effects of microtissue architecture on hiPSC-CM survival, graft vascularization, immune responses, and functional integration. This approach is designed to promote vascular network formation and integration, enhance cardiac microtissue engraftment, and attenuate inflammatory responses for potential therapeutic applications.

fluorescence signal from GFP-labeled ECs (Figure 2). Vascular microtissues consisting of human umbilical vein ECs (HUVECs) and DPSCs[29] retained their shape and adhered to the pillars (Figure 2A). At least 3 different tissue constructs were seeded for each design, demonstrating reproducible tissue shapes (Figures 2C–2E).

A consistent cellular alignment was observed in the duo-pillar designs as assessed by intrinsic GFP signal and adherens junction (VE-cadherin) labeling. In contrast, both GFP and VE-cadherin expression in the designs with three or four pillars were less organized (Figure 2A), with a lower success rate of tissue formation (Figure 2B). Consequently, designs with three or four pillars were eliminated from further experiments. There was no significant difference in propidium iodide (PI) staining after normalizing it to the DAPI signal, indicating minimal cell damage due to the harvesting process (Figures 2F and 2G).

## Production and characterization of cardiac microtissues with duo-pillar designs

Cardiac microtissues with a CM to cFB ratio of 10:1, were evaluated in the duo-pillar designs following the same protocol used for vascular microtissues with troponin T (TnT) expression employed to evaluate sarcomeric alignment (Figures 3B and 3C). Tissues formed in the wells without pillars served as controls (Figure 3A). The tissues in both the “eight” and “candy” shaped wells exhibited higher cellular alignment compared with other designs (Figure 3D) with a consistently higher success rate of tissue formation (Figure 3E). Success is defined as the tissue compacting and stably adhering to the pillars in the mold. Two main modes by which failures occur are: (1) lack of compaction, i.e., the cells fail to undergo the cell/gel compaction process, leading to a lack of condensation around the pillars, and (2) detachment from a post at the end of cultivation (Figure S6). Despite these differences, no variations were observed in the tissue’s electrical excitability, as quantified by excitation threshold (ET) and maximum capture rate (MCR) (Figures 3F and 3G).

Tissue contractile forces and dynamics were quantified using a calibration curve established by a mechanical tester (Figure S2). By tracing the displacement of the pillar tops (Figure 3H), it was determined that tissues formed in the candy-shaped wells exhibited higher contractile forces and shorter contractile durations compared with other designs (Figures 3I and 3J).

## Microtissues support improved *in vitro* vessel network formation

For *in vitro* vascularization modeling, we used the well-established co-culture of ECs and DPSCs.[29] At days 7 and 14 post-seeding, vascularization of the dispersed cell (CM/EC/DPSC) group was poor as indicated by the discontinuous structures visualized in the GFP channel (Figure 4A), consistent with our previous findings.[29] In contrast, the microtissue/EC/DPSC group exhibited the formation of continuous, tube-like structures throughout the fibrin domes. The vascular networks surrounding microtissues were similar to those observed in EC/DPSC controls (Figure 4A). Over the entirety of the 14 day culture period, the microtissue/EC/DPSC group continued to show longer and more interconnected vessels as demonstrated by increased vessel junction density, increased average vessel length, and reduced lacunarity in this group (Figures 4B–4D).

The intricate vascular network within the cardiac microtissues was further evidenced by VE-cadherin-positive tubular structures interwoven throughout these tissues, on day 14 of culture (Figure 4E). In microtissues, CMs were tightly organized into an oval shape. In contrast, the dispersed CM/EC/DPSC group

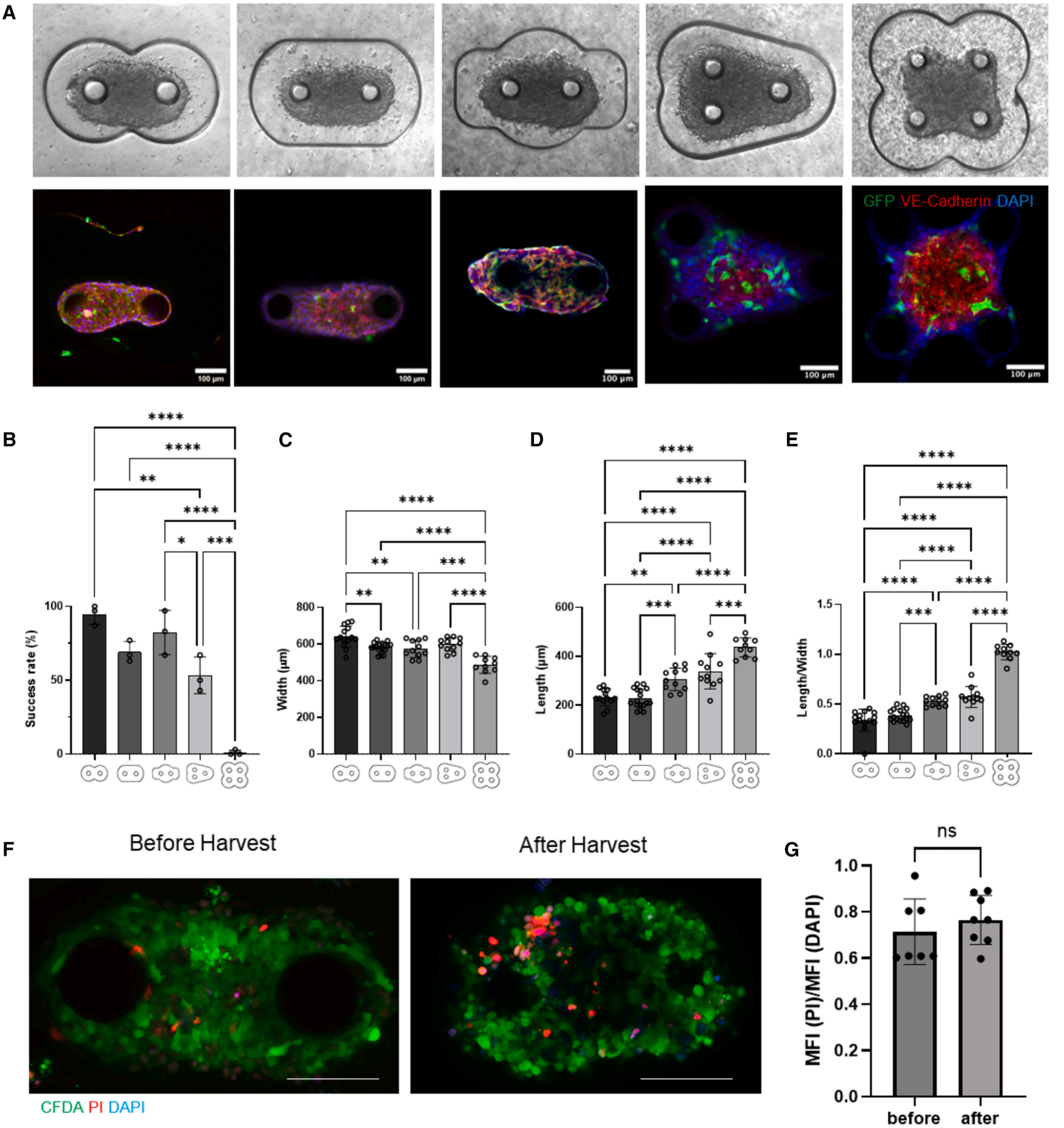

**Figure 2. Vascular microtissue formation in PDMS molds with various designs**

Microtissues were created with ECs (GFP-HUVECs) and DPSCs at a 5:1 ratio.

(A) Bright-field (top row) and confocal (bottom row) images demonstrate tissue morphology and alignment on five different mold designs. Confocal images show GFP expression in ECs (green), VE-cadherin staining (red), and DAPI nuclear staining (blue). Scale bar, 100 µm.

(B–F) (B) The success rate of tissue formation (wrapping around all posts) was compared among groups, with tissues from two pillar designs having consistently better survival rates than three or four-pillar designs. The (C) width, (D) length, and (E) aspect ratio of the formed microtissues were compared among the five groups. After 7-day tissue compaction, microtissues were harvested for downstream applications. Live/dead staining (F) demonstrates live cells (CFDA, green) and dead cells (PI, red). Scale bar, 0.1 mm.

(G) CFDA/PI quantification was performed on microtissues before and after harvest from PDMS molds 7 days post-seeding. Data are represented as mean ± SD, $n \geq 3$. $^{****}p < 0.0001$, $^{***}p < 0.001$, $^{**}p < 0.01$, $^{*}p < 0.05$.

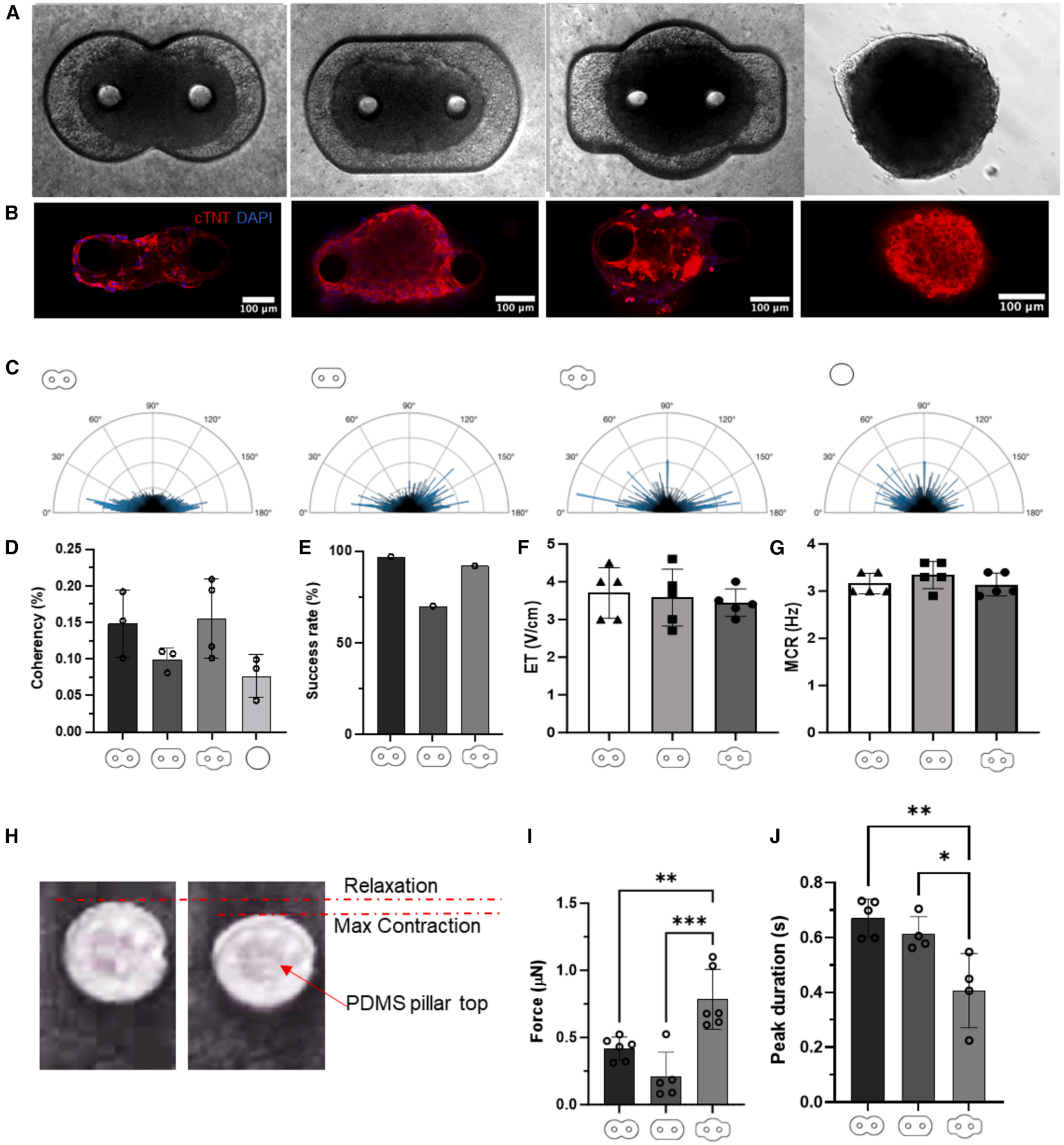

**Figure 3. Cardiac microtissue formation in PDMS molds with duo-pillar designs**

(A and B) (A) Bright-field (top row) and (B) confocal (bottom row) images demonstrating tissue morphology and alignment on three duo-pillar designs and spheroids. Scale bar, 100 μm.

(C) Representative histography of fiber direction within microtissues.

(D–G) (D) Fiber alignment within microtissues was quantified using coherency (percent of structures along a computed dominant direction). Tissue formation success rate (E) and electrical properties such as (F) ET and (G) MCR were quantified.

(H–J) (H) Pillar movement was correlated to (I) contractile forces and (J) dynamics for different pillar designs. Data are represented as mean ± SD, $n \geq 3$. $^{****}p < 0.0001$, $^{***}p < 0.001$, $^{**}p < 0.01$, $^{*}p < 0.05$.

See also Figure S2.

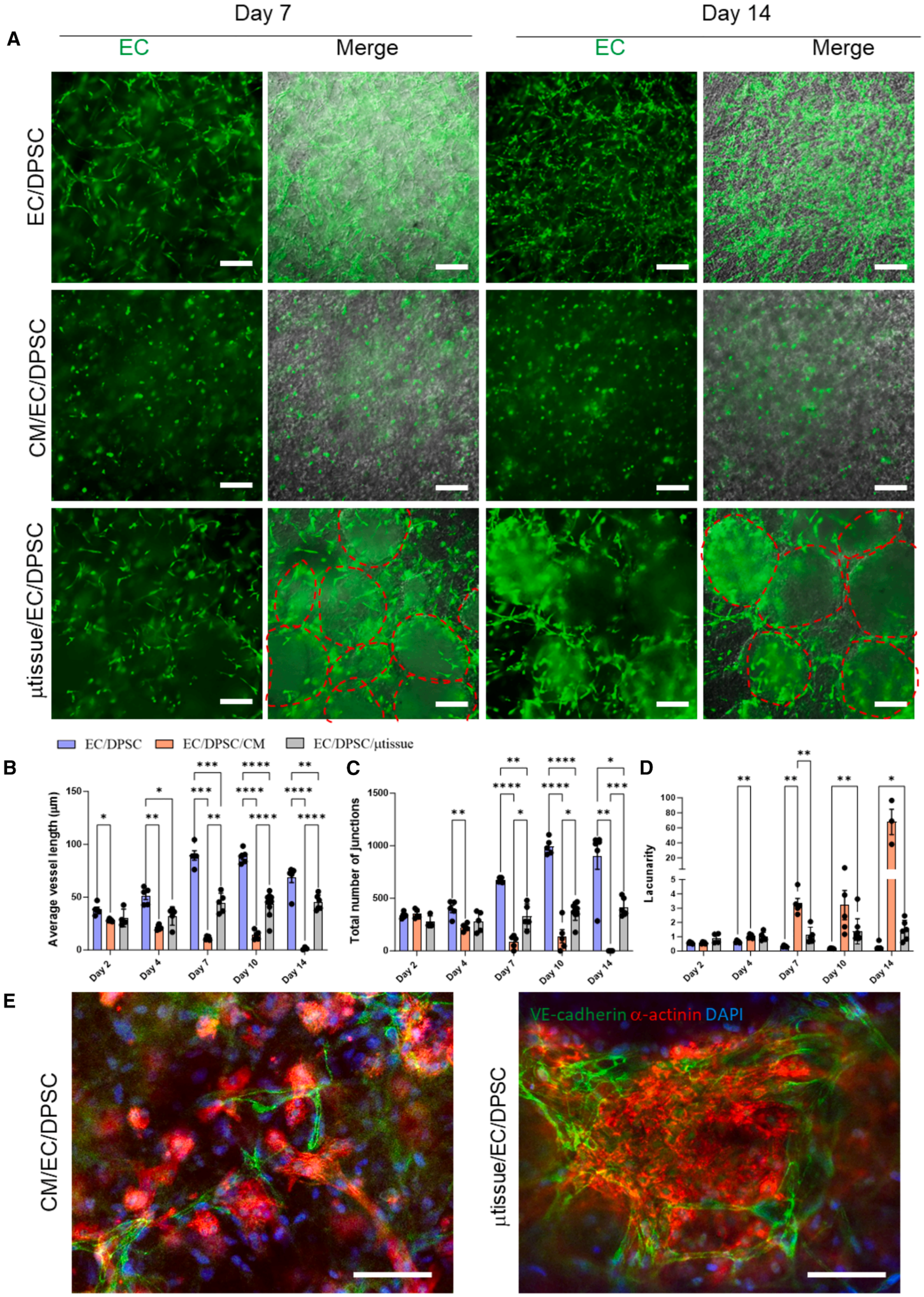

*(legend on next page)*

showed scattered CMs with discontinuous vascular fragments (Figure 4E).

### Microtissues enable creation of large, stable, and electrically active cardiac tissues *in vitro*

To demonstrate the utility of microtissues in scaleup of tissue size *in vitro*, we designed a customized bioreactor to allow for creation of large vascularized cardiac tissues from either dispersed CM or microtissues (Figure S3). This bioreactor utilizes two opposing PDMS tubes that serve as tissue anchors, a perfusion inlet and outlet, and force sensors (Figures S3A–S3E). For seeding, fibrin hydrogel domes were prepared as previously described,[30] carrying either dispersed cells (CM/EC/DPSC) or microtissues (microtissue/EC/DPSC) and seeded into the bioreactor, followed by fibrin hydrogel to fill the large reservoir in the bioreactor (Figure S3F). Upon remodeling over the subsequent 7 days, the tissues in the dispersed CM/EC/DPSC group were significantly more compacted and partially detached from the pillar. In contrast, the tissues in the microtissue/EC/DPSC group remained intact and wrapped around the PDMS tubes creating a large contractile structure (Figure S3G). Electrical excitability was also significantly improved in the microtissue/EC/DPSC group (Figures S3H and S3I).

### Microtissues improve hiPSC-CM survival and omental engraftment, modulate the inflammatory response, and promote vascular ingrowth *in vivo*

To evaluate if microtissues enable increased retention of hiPSC-CMs *in vivo* when compared with dispersed cells, we implanted either dispersed cells or microtissues encapsulated in fibrin hydrogel carrier into the greater omentum of adult male and female athymic *rnu/rnu* rats for 7 days (Figure 5A). Omentum is a highly vascularized structure with key biological functions in immune regulation and tissue regeneration.[31] We envisioned that this blood vessel-rich environment would eliminate hypoxia and serve as an *in vivo* incubator to induce vascularization and subsequent engraftment of our transplanted microtissues. Hematoxylin and eosin (H&E) and cardiac TnT immunostaining of the tissue explants revealed survival and engraftment of microtissues in the omental fat, which appeared to have aggregated into tissue clusters (Figure S4A); CMs in these microtissues showed striations (Figure 5B). In contrast, few if any CMs were identified in the omental fat of the dispersed CMs group (Figure 5B). To confirm the accuracy of our findings, we have examined low-power fluorescent microscopy images of multiple omental sections from animals receiving either microtissues or dispersed CMs. This analysis confirmed the lack of TnT-positive staining throughout the entirety of multiple fixed omental sections in animals receiving dispersed CMs, whereas this staining is clearly visible in omental samples with transplanted microtissues (Figure S7). These findings were further confirmed upon assessment of the electrical excitability of explanted omental microtissue grafts: average ET was 3.24 V/cm (Figure 5C); the average MCR was 3.20 Hz (Figure 5C) consistent with the *in vitro* pre-implantation values (Figures 3F and 3G). In contrast, none of the omental tissues containing dispersed CMs could be excited by an electrical field strength of up to 24 V/cm and all were deemed non-beating (Figures 5C and S4B–S4D). These findings are consistent with the immunofluorescence (IF) staining that showed only minimal hiPSC-CM retention in the dispersed cell group (Figure 5D). Microtissues showed evidence of the improved ingrowth of omental vasculature compared with dispersed CMs as quantified by the number of rat CD31+ vessels (Figure 5E), lower infiltration of total macrophages (CD68+) (Figure 5F), and the enhanced presence of pro-regenerative macrophages (CD206/CD68 ratio) (Figure 5F). The ratio of CD206+ to CD68+ macrophages in omental samples containing microtissues was 1.59, suggesting that the majority of recruited inflammatory cells adopted an M2, or pro-healing, phenotype (Figure 5F). In contrast, the ratio of CD206+ macrophages to CD68+ macrophages was only 0.71 in omental samples in which hydrogels with dispersed CMs were implanted (Figure 5F), suggesting that other pro-inflammatory (M1) macrophage phenotypes may be recruited by these individual cells.

To further assess the impact of non-myocytes on *in vivo* vascularization and engraftment of microtissues, we implanted dispersed CM/EC/DPSC vs. microtissues/EC/DPSC. We saw a universal loss of all transplanted GFP-HUVECs 7 days following omental transplantation (Figure S5A). There was no statistically significant difference in ET and MCR between omental samples containing microtissues and microtissues/ECs/DPSCs (Figure S5B), indicating that the addition of non-myocytes for the purpose of stromal support and graft vascularization does not negatively impact electrical excitability. Consistent with the previous results, the explants from the dispersed CMs/ECs/DPSCs group contained no visible CMs and could not be electrically excited (Figures S5A–S5C). Moreover, cardiac microtissues with added GFP-HUVECs and DPSCs did not exhibit significantly more vascular ingrowth from the host (rat CD31+) omental vasculature when compared with microtissues lacking non-myocytes (Figure S5D). This suggests that the addition of dispersed ECs and stromal cells is not necessary for and does not advance *in vivo* graft vascularization. Interestingly, omental tissues with dispersed CMs/ECs/DPSCs had the largest number of associated CD31+ vessels (Figure S5D), likely secondary to the robust inflammatory response elicited by multiple dispersed cell populations (Figures S5A–S5E), albeit with a complete lack of CMs and non-contractile grafts (Figures S5A–S5C).

Collectively, these findings show that cardiac microtissues promote host endothelial ingrowth, while attenuating inflammatory

**Figure 4. The vascular network regressed when co-cultured with dispersed CMs but remained stable when co-cultured with cardiac microtissues**

(A–D) (A) Morphology of the vascular network (visualized with GFP-HUVECs) at days 7 and 14 using bright-field and fluorescent microscopy. Scale bar, 200 μm. Average vessel length (B), total number of junctions (C), and lacunarity (D), a measure of the distribution of gaps of different sizes in a fractal or multi-scale object, were quantified to compare vessel network formation among EC/DPSC, CM/EC/DPSC, and microtissue/EC/DPSC groups.

(E) Confocal images demonstrating vascular network morphology (VE-cadherin, green) of dispersed CMs and cardiac microtissues (α-actinin, red) with nucleus counterstaining (DAPI, blue). Scale bar, 100 μm. Data are represented as mean ± SD, $n \geq 3$. ****$p < 0.0001$, ***$p < 0.001$, **$p < 0.01$, *$p < 0.05$.

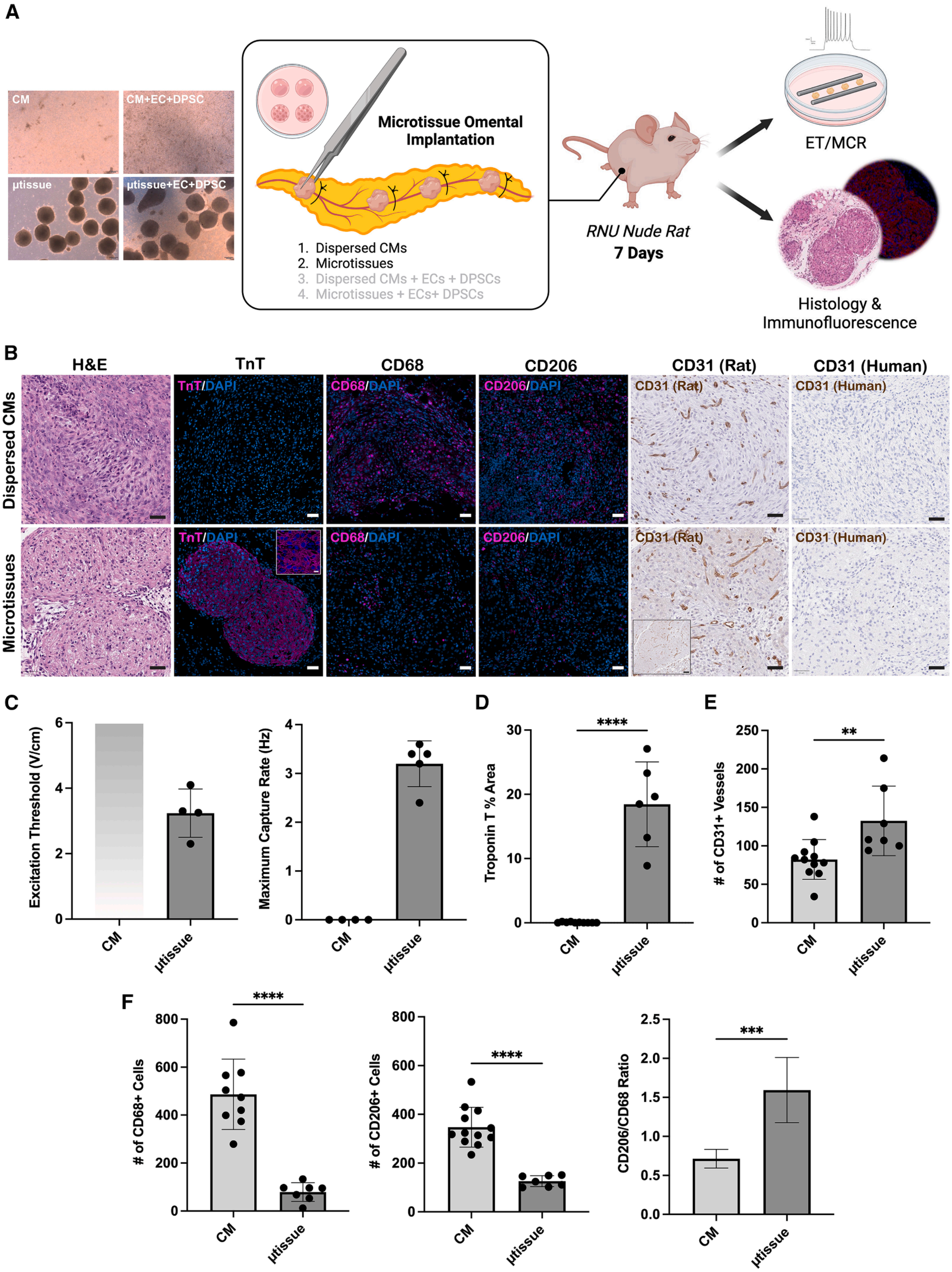

**Figure 5. Microtissues improve hiPSC-CM survival and omental engraftment, modulate the omental inflammatory response, and promote vasculature ingrowth**

(A) Schematic of omental implantation. Fibrin hydrogels containing either dispersed CMs, microtissues, dispersed CMs + ECs + DPSCs, or microtissues + ECs + DPSCs were transplanted onto the omentum of adult athymic *rnu/rnu* rats with each animal receiving each group in four different quadrants. Bright-field images of these hydrogels prior to surgical implantation are shown. 1 week following implantation, omental tissues were removed for contractility assessment and histological/immunohistochemical studies.

(legend continued on next page)

response to the transplant, to generate functional, vascularized grafts with excellent CM retention, preserved architecture, and stable contractile properties and that this response is not dependent on the addition of non-myocyte cell populations.

## Microtissues enable *in vivo* omental engraftment via downregulation of the YAP/TAZ pathway in CMs and associated non-CM cell populations

Yes-associated protein (YAP) and its transcriptional coactivator PDZ-binding motif (TAZ) are key effectors of the Hippo signaling pathway that have been shown to regulate the switch from CM proliferation to maturation during cardiac regeneration.[32] They are also involved in the pathogenesis of MI through multifaceted effects on cFBs[33] and serve as important regulators of macrophage-mediated pro-inflammatory or reparative responses post-MI.[34] To understand the mechanism behind how microtissues modulate the inflammatory response to improve hiPSC-CM survival and omental engraftment, we evaluated the expression of the YAP1 protein in fibrin domes containing dispersed cells (CMs/EC/DPSC) or microtissues (microtissues/EC/DPSC), as well as its expression in matching omental samples (Figure 6A). Importantly, microtissues contain added fibroblasts which may influence the responses. YAP1 expression was significantly decreased in microtissue-associated non-CM cell populations in both *in vitro* and *in vivo* samples when compared with non-CM cell populations of dispersed cell groups (Figure 6B). There was no statistically significant difference between YAP1 expression in dispersed CMs and the microtissue-associated CMs *in vitro* (Figure 6B). Remarkably, when compared with microtissues, significantly more CMs and non-CMs in the dispersed cell group demonstrated YAP1 activation *in vitro* as quantified by nuclear localization (Figure 6C). Upon omental transplantation, the vast majority of dispersed CMs were lost; in contrast, CMs in microtissues remained with the vast majority of YAP1 expression localized to their cytoplasm indicating inactivation (Figure 6A). Examination of the non-CM cell populations *in vivo* (TnT-negative cells such as cFBs, ECs, and omental macrophages) revealed that those associated with microtissues had significantly decreased YAP1 nuclear localization, compared with non-CMs in the dispersed cell group (Figure 6C). These results suggest that a reduced YAP activation in non-CM cell populations (cFBs, ECs, and DPSCs) in microtissues *in vivo* may be responsible for their reduced inflammatory phenotype and ultimately lead to the improved hiPSC-CM survival observed with microtissues following *in vivo* transplantation.

## Microtissues promote *in vitro* vascularization by reducing cell death and cytotoxicity, inducing angiogenic cytokines, and decreasing inflammatory markers

We further hypothesized that the differences in secretome between the dispersed cells and microtissues were responsible for the differential outcome in cardiac tissue grafting, vascularization, and macrophage activation between the two groups. *In vivo*, non-myocytes are abundant, significantly contributing to the secretome. To better mimic this non-myocyte presence in *in vitro* studies, supernatant was collected from the dispersed cell CM/EC/DPSC and microtissue/EC/DPSC groups on day 10 for multiple assessments. First, lactate dehydrogenase (LDH) release was assessed, a common marker for cell damage and death.[35] A lower LDH level was observed in the microtissue/EC/DPSC group compared with the dispersed CM/EC/DPSC group, suggestive of significantly lower levels of cell damage and death (Figure 7A). The secretion of cytotoxicity markers, the cell-free mitochondrial DNA (mtDNA) evaluated by the levels of NADH-ubiquinone oxioreductase chain 1 (ND1) and 4 (ND4), indicated a significantly lower release in the microtissue/EC/DPSC group compared with the dispersed cell group (Figures 7B and 7C). Collectively, these data indicate that cell damage and death in vascularized cardiac tissues are decreased when microtissues are incorporated in place of dispersed CMs. It may be plausible that the lack of tissue architecture and resulting detachment of dispersed CMs from their surrounding extracellular matrix (ECM) is responsible for the increased cell death, release of cell contents such as cell-free mtDNA that is known to promote inflammation[36] and consequent vascular regression noted in these samples.

We analyzed the proteomic profile of culture supernatants from *in vitro* experiments, comparing protein hits associated with apoptosis, necrosis, and pyroptosis. Notably, a great number of protein hits corresponded to apoptotic hallmarks (Figures 7F and S6), suggesting that apoptosis, and not necrosis or pyroptosis, may be the dominant form of cell death. In addition, we identified cytochrome *c* (CYCS) and high mobility group box 1 (HMGB1), known damage-associated molecular patterns (DAMPs) linked to tissue damage and hallmarks of both necrosis and pyroptosis pathways (Figure S6). Additional markers were detected for the necrosis reactome but were absent for pyroptosis pathways (Figure S6), consistent with the finding of elevated LDH, ND1, and ND4 release (linked to Toll-like receptor [TLR] signaling[37]) in the dispersed cell group (Figures 7A–7C). However, since supernatants were collected on day 10 post-seeding,

(B and C) (B) Representative H&E, TnT, CD68, CD206, and CD31 (rat and human) immunostaining images of omental samples. TnT inset shows CM striations within microtissues; CD31 inset shows the architecture of microtissue aggregates. Microtissues demonstrated improved graft survival and a markedly reduced inflammatory response compared to tissues containing dispersed CM; note the ingrowth of rat omental vasculature into microtissues. Scale bar, 50 μm. Inset scale bar, 20 μm for TnT and 100 μm for CD31; (C) ET and MCR measurements for omental tissues immediately post-explanation (mean ± SD, $n \geq 4$). None of the samples containing dispersed CMs were beating.

(D) Quantification of TnT area fraction demonstrated survival and engraftment of microtissues in the omental fat; dispersed CMs showed poor persistence at 7 days.

(E) Quantification of rat CD31+ vessels.

(F) Quantification of CD68+ macrophages, CD206+ macrophages, and the ratio of CD206+ to CD68+ macrophages. Scale bar, 50 μm. All graphical data are represented as mean ± SD, $n \geq 6$. ****$p < 0.0001$, ***$p < 0.001$, **$p < 0.01$.

See also Figures S4 and S5.

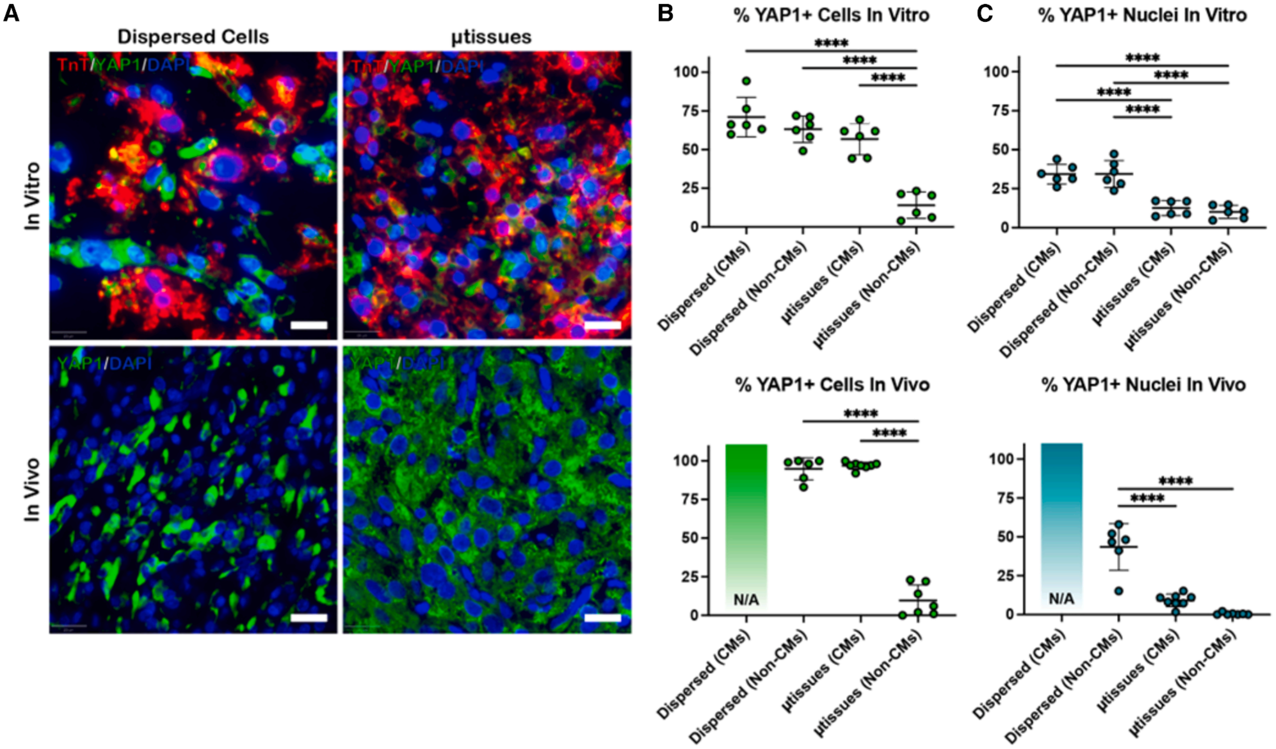

**Figure 6. Microtissues enable tissue engraftment via downregulation of YAP/TAZ pathway in both CMs and surrounding non-CM cell populations**

(A) Representative images of TnT and YAP1 immunostaining performed on fibrin hydrogels seeded with dispersed CMs/ECs/DPSCs or microtissues/ECs/DPSCs (top row) and YAP1 immunostaining of corresponding omental samples (bottom row).

(B) Quantification of the percentage of YAP1+ cells in both *in vitro* and *in vivo* samples. Expression was evaluated in CM and non-CM cell fractions. There were no remaining dispersed CMs in *in vivo* omental samples.

(C) Quantification of the percentage of YAP1+ nuclei in both *in vitro* and *in vivo* samples. Expression was evaluated in CM and non-CM cell fractions. There were no remaining dispersed CMs in *in vivo* omental samples. Scale bar, 20 μm. Data are represented as mean ± SD $n \geq 3$. $^{****}p < 0.0001$.

it is possible that certain pyroptosis and necrosis-related proteins are no longer detectable at this time point.

To explore the cytokine release profile, the supernatant collected on day 14 was analyzed using an antibody array targeting 507 cytokines (Figure 7D). Among the most differentially released cytokines, we detected several pro-angiogenic cytokines including placenta growth factor (PlGF)[38,39], endocan,[38,39] and angiopoietin-2,[40] which were significantly elevated in the microtissue/EC/DPSC group when compared with the dispersed CM/EC/DPSC group. Similarly, many cytokines that are elevated in the microtissue/EC/DPSC group in comparison with the microtissue-only group may promote angiogenesis via the increased production of vascular endothelial growth factor (VEGF) (ErbB2[41]), stimulation of EC survival (angiopoietin-like 1[42]), proliferation, and migration (TWEAK,[43] leptin,[44] EG-VEGF/PK1,[45] and sonic hedgehog [Shh N-terminal][46]), as well as the stabilization of the sprouting vasculature network (CXCR3[47]) (Figure 7E).

On the other hand, elevation of cardioprotective cytokines IP-10[48] and β-catenin,[49] as well as the decrease of inflammation-related TLRs TLR3 and TLR4,[50] which are also receptors for cell-free mtDNA, were identified in the microtissue/EC/DPSC group compared with the dispersed cell group. The reduction of other inflammatory markers (Table 1), including interleukin-31 receptor A (IL-31 RA),[51] interleukin (IL)-2 R beta/CD122,[52] OX40 ligand,[53] neutrophil activating peptide 2 (NAP-2),[54] and S100A10,[55] indicated a diminished inflammatory state in the microtissue/EC/DPSC group compared to the dispersed cell group. Analysis of gene ontology bioprocess and the reactome pathway (Figure 7F) also confirmed significant downregulation in the immune response, IL-12 production, and apoptotic signaling pathway. Importantly, compared with the microtissue-only group, the microtissue/EC/DPSC group exhibited elevated levels of inflammatory cytokines, including IL-23[56] and IL-3.[57] These cytokines play crucial roles in immune modulation of EC activation, which often precedes vascular remodeling.

The supernatant isolated from cultured tissues on day 10 underwent proteomic analysis, which revealed that only four secreted proteins were significantly upregulated in the microtissue/EC/DPSC group compared with the dispersed CM/EC/DPSC group, while the remainder of differentially expressed proteins were downregulated (Figure S7). Among the upregulated proteins were MYH6 and ATP5A1, which are primarily associated with the cardiac contractile machinery and mitochondria respiration[65,66] (Figure 7G). Protein interaction network analysis

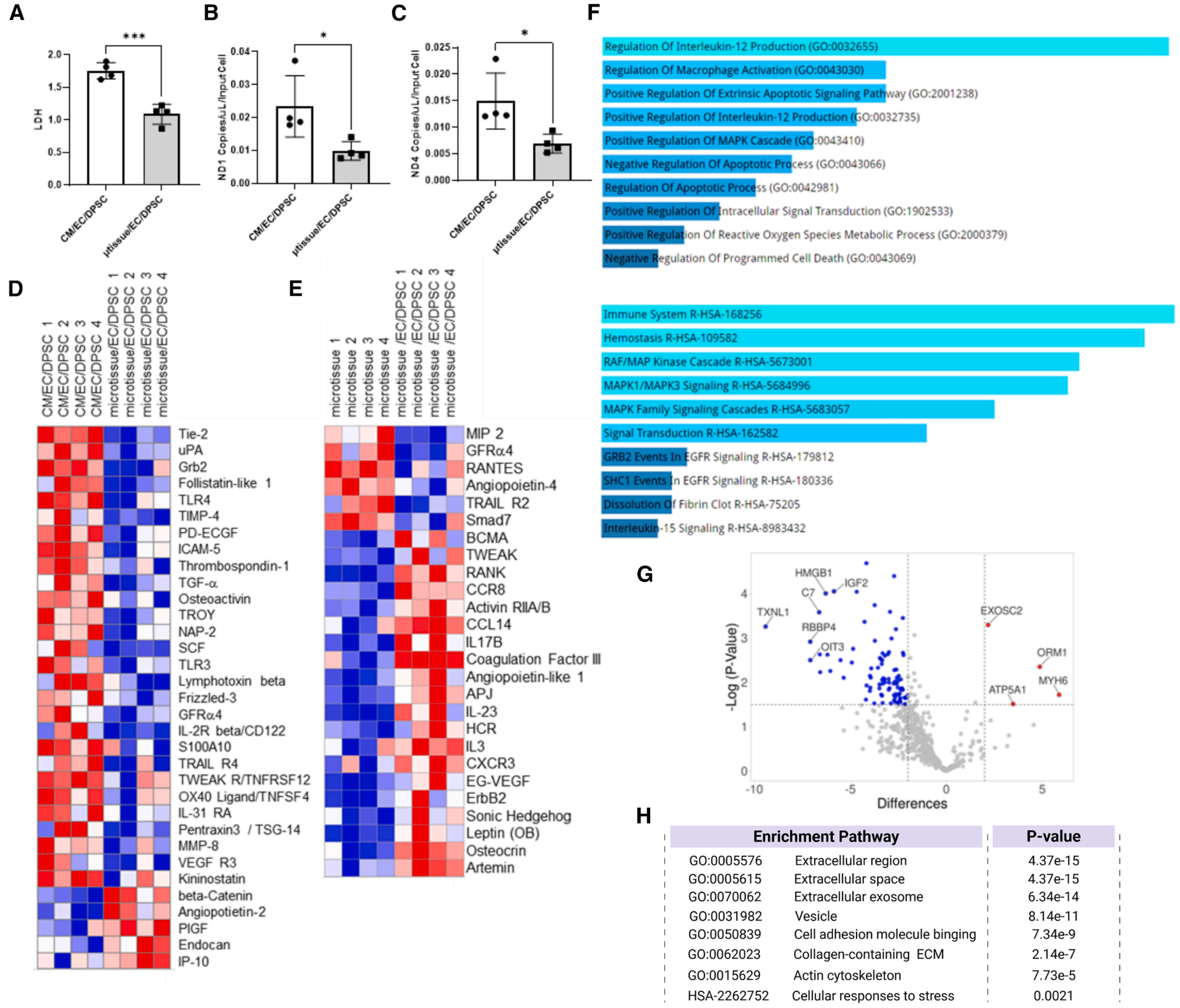

| Enrichment Pathway | | P-value |
|---|---|---|
| GO:0005576 | Extracellular region | 4.37e-15 |
| GO:0005615 | Extracellular space | 4.37e-15 |
| GO:0070062 | Extracellular exosome | 6.34e-14 |
| GO:0031982 | Vesicle | 8.14e-11 |
| GO:0050839 | Cell adhesion molecule binging | 7.34e-9 |
| GO:0062023 | Collagen-containing ECM | 2.14e-7 |
| GO:0015629 | Actin cytoskeleton | 7.73e-5 |
| HSA-2262752 | Cellular responses to stress | 0.0021 |

**Figure 7. Secretome analysis indicates that microtissues reduce cell death, decrease inflammation from mtDNA, and improve angiogenesis**

(A–E) (A) LDH levels and cell-free mtDNA, detected as (B) ND1 and (C) ND4, were quantified and compared between dispersed CM/EC/DPSC and microtissue/EC/DPSC groups. Using an antibody array targeting 504 cytokines, significant differences in cytokine levels were assessed and compared between (D) dispersed CM/EC/DPSC and microtissue/EC/DPSC samples, as well as (E) between micro-tissue only samples and microtissue/EC/DPSC samples.

(F) Gene Ontology and reactome analysis demonstrated downregulated immune response and apoptotic signaling in the microtissue/EC/DPSC group.

(G) Secretome (proteomic) analysis using day 10 supernatants presented an asymmetrical volcano plot, indicating most cytokines were downregulated in the microtissue/EC/DPSC group when compared with the dispersed CM group.

(H) Pathway analysis shows downregulation of vesicle activity, extracellular activity, reduced stress, and actin activity.

Data are represented as mean ± SD, $n \geq 3$. $^{***}p < 0.001$, $^{*}p < 0.05$.

See also Figures S6 and S7.

of the downregulated proteins suggests they are primarily associated with immune system activation, vesicle regulation, extracellular stress, and actin activity (Figures 7H and S7).

## DISCUSSION

Our study underscores the advantages of using microtissues in place of dispersed CMs for both establishing vascular networks in engineered cardiac tissue *in vitro* and enhancing engraftment and vascularization of cardiac tissues *in vivo*, while attenuating inflammation and promoting pro-regenerative environment.

Many devices introduce tension via topographical features during tissue formation, improving CM organization.[67–72] This enhances contractile behavior through synchronized CM activity and promotes the development of intracellular structures such as sarcomeres vital for contractile performance. Our *in vitro* results demonstrate that geometric shapes and pillar arrangements critically influence myofiber alignment, tissue architecture, and

**Table 1. Summary of significantly different cytokines**

| Name | Function | Ref |
|---|---|---|
| IL-31 receptor A (IL-31 RA) | involved in inflammatory signaling, contributes to conditions such as pruritus | Feng et al.[51] and Kabashima and Irie[58] |
| IL-2 R beta/CD122 | part of the IL-2 receptor, crucial for T cell proliferation and immune responses | Arenas-Ramirez et al.[52] and Ross and Cantrell[59] |
| TRAIL R4 (TNFRSF10D) | involved in the regulation of apoptosis and it can influence inflammation | McGrath et al.[60] |
| TWEAK R (TNFRSF12) | regulates various cellular processes including inflammation, cell proliferation, and apoptosis | NCBI[61] |
| OX40 ligand (TNFSF4) | costimulatory molecule involved in T cell activation and inflammatory responses | Ishii et al.[53] and Balan et al.[62] |
| Neutrophil activating peptide 2 (NAP-2) | chemokine involved in neutrophil activation and chemotaxis, contributing to inflammation | Smith et al.[54] and Brown et al.[63] |
| S100A10 | involved in the regulation of various inflammatory processes | O'Connell et al.[55] and Okura et al.[64] |

overall functional performance of the microtissues. Designs with 3 and 4 pillars created a planar distribution of tension, resulting in less cellular alignment. Instead, the duo-pillar microtissues exhibited superior uniaxial cellular alignment compared with other designs and controls. This is expected, as many heart-on-a-chip devices utilize uniaxial strain by incorporating duo-wires,[67,68] pillars,[69–72] or single sutures centrally[73] to encourage cardiac functional maturation. The candy-shaped well design outperformed other configurations, as tissues exhibited stronger contractile forces and shorter beating durations, likely due to a larger cellular area localized to the center of the well. By constraining microtissue size to a width and depth of 300 μm, we ensured adequate oxygen and nutrient diffusion into the microtissues to address their high oxygen demand. This approach maintains tissue viability and functionality by effectively preventing the formation of necrotic cores, a common limitation in the engineering of thicker and larger tissues.[74]

Many groups have previously seeded CMs around two posts to control cellular alignment and create anisotropic, contractile cardiac microtissues.[69,75–77] Larger tissue structures with spatial control of the magnitude and direction of contractile force could be assembled from these smaller microtissue subunits.[78] Other studies have reported improved cell retention with microtissues in both animal models[79–81] and an early-stage clinical trial.[82]

A unique aspect of this work is that cultivation in the format of geometrically aligned microtissues reduced the inflammatory secretome, which is critical for successful vascularization *in vitro* and grafting *in vivo*. Another unique aspect of our study is the involvement of microtissue architecture in the inactivation of the YAP pathway and downstream attenuation of the inflammatory profile of non-myocytes.

Several previous studies, e.g., Landau et al.[30] and Rajasekar et al.,[83] obtained optimal vascularization of tissues *in vitro* using ECs and stromal support cells in a 5:1 ratio. In this study, we used the same ratio for generating vascularized microtissues. DPSCs were chosen as supporting cells as they have previously been shown to be essential for the stabilization of vascular networks *in vitro*.[7,8]

The specific ratio of CMs to cFBs was informed by our previous work on the Biowire II platform, which established this ratio as optimal for the generation of contractile trabeculae of cardiac muscle from iPSC-derived CMs.[28] The efficacy of this ratio has been demonstrated via numerous subsequent disease modeling studies by our groups and others.[84–86]

To elaborate, compared with dispersed cells, microtissues co-cultured with ECs and DPSCs showed enhanced vessel network formation, as evidenced by the formation of continuous, tubular structures throughout the cardiac microtissues. This improvement is likely due to the stable microenvironment created by microtissues relative to dispersed CMs. By pre-forming microtissues in the PDMS mold for 7 days, optimal cardiac tissue remodeling can be achieved before co-culturing these tissues with ECs and DPSCs. This is supported by significantly reduced cell death quantified by lower LDH levels, and decreased cell-free mtDNA fragments. Moreover, cytokine profile analysis revealed reductions in TLR3 and TLR4, hallmarks of mtDNA-driven inflammation pathways, which is consistent with decreased mtDNA levels observed in the microtissue group.[36] Correspondingly, the lower levels of TRAIL-R4[87] and TWEAK R[88] also suggest decreased activation of nuclear factor κB (NF-κB), another key protein in mtDNA-driven inflammation pathways. Overall, microtissues allowed for the development of a microenvironment that downregulated pathways responsible for cell death and tissue damage.

The reduction of inflammatory markers (Table 1) including IL-31 RA, IL-2 R beta,[89] OX40 ligand, NAP-2, and S100A10 in the microtissue group also indicated the downregulation of the inflammatory cascade, which created a microenvironment that mitigates immune-mediated tissue damage and is conducive to vessel formation and stabilization. Decreases in IL-31 RA[90] and NAP-2[91] suggest a diminished local inflammatory response, while OX40 ligand is present on activated ECs[92]; its lower level is indicative of reduced EC activation. Collectively, these changes enhance the viability and functionality of microtissues by reducing the risk of immune rejection via the elicited inflammatory response.

Cytokine profile analysis additionally revealed elevated levels of pro-angiogenic factors, including PIGF, endocan, and angiopoietin-2, alongside reduced inflammatory markers in the microtissue/EC/DPSC group. More specifically, angiopoietin-2, primarily expressed in ECs, enhances vessel destabilization to facilitate stimulation of sprouting and vascular network remodeling through external stimuli such as hypoxia.[93] Endocan is expressed as a marker of tip ECs to mediate vessel sprouting during neoangiogenesis.[94] TIMP4, an inhibitor of capillary EC migration,[95] was also downregulated in the microtissue group. This, combined with the upregulation of endocan and angiopoietin-2, suggests the active formation of a sprouting vascular network. PlGF-1 is a well-known angiogenic cytokine, which antagonizes VEGF-induced angiogenesis by the formation of functionally inactive PlGF-1/VEGF heterodimers.[96] The antagonization explains the downregulation of VEGF receptor 3.[97] Kininostatin, an angiogenic inhibitor that inhibits proliferation and induces apoptosis of human ECs,[98] was also reduced in the microtissue group.

The other elevated cytokines, β-catenin and IP-10, are more closely linked to cardiac tissue function. The Wnt signaling pathway, with β-catenin as a key component, is critical during cardiac embryonic development.[99] Recent data suggest that β-catenin plays a complex role in the metabolic maturation of the perinatal heart, helping establish adult patterns of glucose and fatty acid utilization.[100] Wnt/β-catenin signaling is critically required for the cFB-mediated repair response following ischemic myocardial injury; components of this pathway have also been shown to be carried in extracellular vesicles (EVs), and have a pro-angiogenic effect by activating Wnt/β-catenin signaling in ECs.[101] Additionally, the upregulation of IP-10 indicates cardiac protective responses during stress,[102] further highlighting the functional benefits provided by microtissue architecture.

It is worth noting that proteomic and cytokine profile analyses were taken from separate tissue batches but presented a consistent and asymmetrical distribution between upregulated and downregulated proteins. Based on the proteomic analysis of the supernatant, extracellular activity, such as EV secretion, was downregulated in the microtissue group. This is consistent with the observed downregulation of cell-free mtDNA, as EVs typically contain substantial amounts of cell-free mtDNA,[103] and with recent data from our group suggesting that CM-derived EVs inhibit vascularization *in vitro*.[104] As cardiac microtissues reached homeostasis before being introduced to the EC/DPSC co-culture, there was less extracellular activity, including ECM secretion, compared with the dispersed CM group. This reduced extracellular activity suggests a stable microenvironment within the microtissues that contributes to enhanced tissue viability and function.

On the other hand, a significant elevation of angiogenic and inflammatory cytokines in the microtissue/EC/DPSC group compared with the microtissue-only group indicates that the presence of dispersed ECs and DPSCs enhances both vascularization and immune-related signaling, contributing to a dynamic and unstable vascular network that could be highly responsive to modulation *in vivo*. This may explain the negligible effects of the presence of ECs/DPSCs on tissue vascularization *in vivo*. In future studies, microtissue containing ECs/DPSCs would facilitate a more stable vascular network and promote homeostatic cell-cell contact, which may hold the potential to decrease the inflammatory signature.

Our *in vivo* studies further evaluated the feasibility of the microtissue approach on cell survival and graft vascularization 7 days post-transplantation. We selected the omentum as the site for tissue implantation as it is a blood vessel-rich environment that serves key immunological functions; moreover, it ensures that hypoxia is not a significant contributor to *in vivo* cell death.[31] Unlike the infarct zone following coronary artery ligation in animal models of myocardial ischemia, which is a highly inflammatory and a poorly vascularized environment, the omentum is a well-vascularized but relatively inflammation-free environment. This enables us to decouple the immunologic properties of the implanted engineered tissues from the inflammatory response occurring in the host implantation site as a result of injury.

Although previous studies show some correlation between successful omental grafting and cardiac implantation,[105] the omental implantation may not be able to fully predict the outcome of cardiac implants, especially for critical features such as functional coupling between implanted and host cells. In this study, the omentum was a suitable preliminary site for testing our hypothesis that isolated single CMs exhibit an inflammatory secretome, which contributes to their lack of *in vivo* engraftment, and that this issue can be mitigated via microtissue cultivation[31,106] It was crucial to select a site that is not hypoxic, as hypoxia can independently impact cell survival regardless of the inflammatory milieu. The omentum provides an optimal *in vivo* environment for microtissue implantation due to its ability to support neovascularization, elicit an immune response, and promote tissue healing and regeneration. These properties have long been recognized in surgical practice, and the omentum has been extensively used for engineered cardiac tissue grafting in previous research.[31,105,107,108] For these reasons, we chose the omentum—a well-perfused, immunologically regulated site—to ensure optimal conditions for addressing our study's main hypothesis.[109]

Cardiac microtissues showed unprecedented persistence and omental engraftment at this early time point (7 days) and retained their contractility when compared with dispersed CMs, most likely secondary to an attenuated inflammatory response and vascular ingrowth from the host omental vasculature. The decreased immune response and increase in the proportion of pro-healing (M2) macrophages in comparison with dispersed CMs is consistent with the cytokine profile analysis, suggesting that microtissues create an anti-inflammatory microenvironment. This may be due to their enhanced maturity; others have demonstrated that hiPSC-CMs matured via long-term culture show improved engraftment and angiogenesis post-transplantation in infarcted rat hearts.[110]

Interestingly, examination of non-CM cell populations revealed that those associated with microtissues had significantly decreased YAP1 nuclear localization compared with non-CM cells surrounding dispersed CMs both *in vitro* and *in vivo*. This is particularly revealing given that YAP1 activation in these cell populations is associated with the orchestration of a fibroinflammatory response by cFBs and endothelial cell-mediated release of pro-inflammatory cytokines.[111,112] Indeed, it has been shown that a strong nuclear presence (i.e., activation) of YAP in cFBs promotes macrophage recruitment and an inflammatory reaction that impairs cardiac function following MI.[113]

YAP activation in macrophages polarizes them toward a pro-inflammatory phenotype and impairs their reparative response; YAP/TAZ deletion has resulted in reduced fibrosis and increased angiogenesis leading to improved cardiac function post-MI.[34] This is corroborated by the increased number of pro-inflammatory macrophages observed in our dispersed CM omental samples. Finally, microtissues (both *in vitro* and those found in omental samples) exhibited decreased YAP1 activation as quantified by reduced nuclear localization. Although nuclear activation of YAP drives CM proliferation through the promotion of cell cycle re-entry, it is the cytoplasmic retention of YAP that is associated with the development of contractile function and energy metabolism characteristic of postnatal CM maturation.[32] This is further confirmed by our proteomics data that demonstrate the upregulation of proteins associated with the cardiac contractile machinery and mitochondrial respiration in microtissues. Conversely, we observed downregulation of the protein YWHAE in media isolated from microtissues—this oncoprotein interacts with YAP/TAZ to regulate cyclin D1 expression and increase cell proliferation.[114]

Although ECs and DPSCs significantly enhance vessel formation when co-cultured with dispersed CMs *in vitro*, these cells were not necessary for microtissue vascularization *in vivo*. Microtissues themselves enhance vessel formation through the upregulation of pro-angiogenic factors. As such, in the future microtissues may offer a novel approach to improving cell-based therapies directed at cardiac remuscularization and functional recovery when injected intramyocardially, with improved tissue vascularization and engraftment compared with isolated CMs, where CM retention is minimal.

In future studies, we plan to investigate whether vessel ingrowth can be enhanced if microtissues are co-cultured with pre-formed luminal networks rather than dispersed ECs prior to transplantation, particularly in ischemic environments such as the heart following MI. Additional limitations of this study could be addressed if the omental implantations continued for 6 weeks or more, to better evaluate if the fibrosis would occur at the microtissue graft periphery. Given the chosen implantation site, it was difficult to quantify what percentage of implanted microtissues remain in the omental fat after 7 days, with future studies requiring tissue homogenization and qPCR for human antigens to enumerate transplanted cell retention. Although it is difficult to precisely match the number of transplanted dispersed CMs and those in microtissues, due to the remodeling of microtissues during *in vitro* culture that impact cardiac cell numbers, the lack of any identifiable dispersed CMs in explanted omental samples strongly suggests that observed differences in CM persistence were secondary to tissue architecture rather than varying transplanted cell numbers. Further work is needed to precisely enumerate YAP activation in sub-populations of non-myocytes, assess its effect on CM proliferation in microtissues, and provide better mechanistic understanding of mechanotransduction in microtissues. *In vivo* formation of fully perfusable vasculature in and around microtissues is required, as well as further microtissue maturation via long-term culture and electrical stimulation as previously described.[28,76]

Recent data suggest functional improvement with epicardially-attached engineered cardiac tissue patches in non-human primates, success which may translate to human clinical trials.[115] We thus envision three principal ways in which microtissues could be delivered to the heart following MI: (1) via direct intramyocardial injection using a shear-thinning gel carrier to facilitate delivery and protect the microtissues as they pass through the needle,[116] (2) via additional cultivation to form a sheet-like structure that can then be sutured to the epicardial surface, and (3) via suspension in a suitable hydrogel and introduction into a conical mold to create a sac-like structure that can be pulled over the heart. In future studies, incorporation of primitive macrophages into microtissues may further improve CM retention and tissue vascularization, consistent with recent reports.[29,85]

## Conclusions

Herein, we show that hiPSC-CMs fashioned into geometrically controlled microtissues can modulate the immune response to ensure significantly improved CM survival and grafting compared with dispersed cells, enabling the formation of large, assembled tissues. Concurrently, we demonstrate that the microtissues enable the creation of robust vascular networks both *in vitro* via co-culture with ECs and DPSCs and *in vivo* by secreting pro-angiogenic factors to stimulate omental vessel ingrowth. We demonstrate the potential of these microtissues to serve as building blocks for contractile grafts that both evade the host inflammatory response and promote vasculature formation, thus offering a promising new approach for cardiac repair and regenerative medicine applications.

## METHODS

### Key resources table

| REAGENT or RESOURCE | SOURCE | IDENTIFIER |
|---|---|---|
| Antibodies | | |
| Mouse anti-α-actinin | Abcam | Cat# 137346 RRID:AB_2909405 |
| Rabbit anti-MLC2v | Abcam | Cat# 79935 RRID:AB_1952220 |
| Mouse anti-troponin-T | Thermo Scientific | Cat# MA512960 RRID:AB_11000742 |
| Mouse anti-CD68 | Thermo Scientific | Cat# 14-0688-82 RRID:AB_11151139 |
| Rabbit anti-VE-cadherin | Abcam | Cat#ab33168 |

(*Continued on next page*)

***Continued***

| REAGENT or RESOURCE | SOURCE | IDENTIFIER |
|---|---|---|
| Goat anti-rabbit Alexa Flour 647 | Thermo Scientific | Cat# A32795 RRID:AB_2762835 |
| Goat anti-rabbit Alexa Flour Plus 555 | Thermo Scientific | Cat# A32732 RRID:AB_2633281 |
| Goat anti-mouse Alexa Flour 647 | Thermo Scientific | Cat# A21240 RRID:AB_2535809 |
| DAPI | Sigma-Aldrich | Cat# D1306 RRID:AB_2629482 |
| CD31 (cross-reactivity to human ECs only) | Dako | M0823 |
| CD31 (cross-reactivity to both human and rat ECs) | Novus | NB-100-2284 |
| CD68 | Abcam | Ab125212 |
| CD206 | Abcam | Ab64693 |
| YAP1 | Thermo Fisher Scientific | PA1-46189 |
| Chemicals, peptides, and recombinant proteins | | |
| Polyurethane casting and potting system | GS polymers | Cat# GSP1552-2 |
| Dow SYLGARD 184 Silicone Encapsulant Clear 0.5 kg Kit | Ellsworth adhesives | Cat#184 SIL ELAST KIT 0.5KG |
| Carbon rods | Ladd Research Industries | Cat# 30250 |
| Critical commercial assays | | |
| RNase-free DNase set | QIAGEN | Cat# 79254 |
| Human L507 array, glass slide | RayBiotech | Cat# AAH-BLG-1-8 |
| LDH cytotoxicity assay | Cayman Chemical Company | Cat# 601170-96 |
| ImmPRESS HRP Horse Anti-Rabbit immunoglobulin G (IgG) Polymer Detection Kit | Vector Laboratories | Cat# MP-7401 |
| Deposited data | | |
| Mass spectrometry proteomics data | The PRIDE partner repository[117] | Identifier PXD055832 |
| Experimental models: Cell lines | | |
| GFP-expressing HUVECs | Angio-Proteomie | Cat#:cAP-0001GFP |
| DPSC—human dental pulp stem cells | LONZA | Cat#: PafT-5025 |
| Human cardiac fibroblasts (cFBs) | PromoCell | Cat#: CC-2904 |
| BJ1D cell line | Gift from Dr. William Stanford, now at Ottawa Heart Institute | N/A |
| Oligonucleotides | | |
| Primer/probe sequence for ND1 and ND4: ND4-F1 5′-CCATTCTCCTCCTATCCCTCAAC-3′; ND4-R1 5′-ACAATCTGATGTTTTGGTTAAACTATATTT-3′; ND4-Probe 5′-FAM/CCGACATCA/ZEN/TTACCGGGTTTTCCTCTTG/3IABkFQ/-3′; ND1-F1 5′-CCCTAAAACCCGCCACATCT-3′; ND1-R1 5′-GAGCGATGGTGAGAGCTAAGGT-3′; ND1-Probe 5′-HEX/CCATCACCC/ZEN/TCTACATCACCGCCC/3IABkFQ/-3′; ND4 + ND1 geneblock—5′-CACGAGAAAACACCCTCATGTTCATACACCTATCCCCCATTCTCCTCCTATCCCTCAACCCCGACATCATTACCGGGTTTTCCTCTTGTAAATATAGTTTAACCAAAACATCAGATTGTGAATCTGACAACAGAGGCTCTCTTCACCAAAGAGCCCCTAAAACCCGCCACATCTACCATCACCCTCTACATCACCGCCCCGACCTTAGCTCTCACCATCGCTCTTCTACTATGAACCCCCCTCCCCATACCCAA-3′ | IDT | N/A |
| Software and algorithms | | |
| Image analysis MATLAB code | Referenced | Landau et al.[118] |
| Other | | |
| TrypLE | ThermoFisher | Cat# 12,605,010 |

(*Continued on next page*)

*Continued*

| REAGENT or RESOURCE | SOURCE | IDENTIFIER |
|---|---|---|
| L-Glutamine | ThermoFisher | Cat# 25,030,081 |
| Transferrin | ROCHE | Cat# 10,652,202,001 |
| Ascorbic acid | Sigma-Aldrich | Cat# A4544-100G |
| ROCK inhibitor Y-27632 | TOCRIS | Cat# 1254 |
| Aprotinin from bovine lung | Sigma-Aldrich | Cat# A3428 |
| StemPro-34 SFM | Life Technologies | Cat# 10639011 |
| EGM2 | PromoCell | Cat# C-22011 |
| Fibroblast growth medium 3 | PromoCell | Cat# C-23025 |
| Aprotinin from bovine lung | Sigma-Aldrich | Cat# A3428 |
| StemPro-34 SFM | Life Technologies | Cat# 10639011 |
| RPMI with L-glutamine | Life Technologies | Cat# 11875-093 |
| B27 plus insulin | Life Technologies | Cat# 17504-044 |
| B27 supplement minus insulin 50× | Life Technologies | Cat# A1895601 |
| mTeSR | Cedarlane | Cat# 05850 |
| 2-Phospho-L-ascorbic acid trisodium salt | Sigma-Aldrich | Cat# 49752 |
| IWP4 | Miltenyi Biotec, Stemgent | Cat# 04-0036 |
| CHIR 99021 | Miltenyi Biotec, Stemgent | Cat# 04-0004 |
| NaOH | Caledon | Cat# 7860-1-70 |
| $NaHCO_3$ | E COM | Cat# SX0320-1 |
| Growth factor reduced Matrigel | Corning | Cat# 354230 |
| DMEM | Thermo Fisher | Cat# 11054-080 |
| Fetal bovine serum (FBS) | Life Technologies | Cat# 12483020 |
| Penicillin-streptomycin | Thermo Fisher | Cat# 15070063 |
| Human fibrinogen | Sigma-Aldrich | Cat# F3879 |
| Human thrombin | Sigma-Aldrich | Cat# T6884 |
| Trypsin/EDTA 0.05% | Life Technologies | Cat#25300054 |
| Low-glucose DMEM | Gibco | Cat#11054020 |
| MEM non-essential amino acids solution (100×) | Thermo Scientific | Cat# 11140050 |
| HEPES | Thermo Scientific | Cat# 15630080 |
| GlutaMAX | Life Technologies | Cat# 35050061 |
| Tetramethylrhodamine isothiocyanate-dextran | Sigma-Aldrich | Cat# T1162 |
| Triton X-100 | BioShop Canada | Cat# TRX777.100 |
| 4-in silicon wafer | University Wafer | Cat# 590 |
| SU-8 2150 | Kayaku advanced Materials | Cat# Y111077 0500L1GL |
| Prolene suture 7-0 | Ethicon | Cat# 8702H |
| Polysorb suture 5-0 | Covidien | Cat# SL690 |
| Protein block | Agilent Technologies | Cat# X090930-2 |
| Fluorescence mounting medium | Agilent Dako | Cat# S302380-2 |
| Titanium microclips (GEM MicroClip) | Synovis Micro Companies Alliance | Cat# GEM2431 |
| MM 24 mounting medium | Leica | Cat# 3801120 |
| DAB | Dako | Cat# K3468 |

## Experimental model and participant details

### *BJ1D CMs*

For cardiac differentiation BJ1D iPSC (male) were routinely maintained in a Matrigel-coated 6-well plate in mTeSR plus media and were differentiated into CMs based on previously reported protocol.[14] Briefly, BJ1D iPSCs were pre-plated in 12-well plate at 0.75 million cells per well and maintained in mTeSR plus media for 24–48 h until 100% confluence. RPMI supplemented with B27 (no insulin), penicillin-streptomycin (pen-strep), and CHIR (8 μM) were added on day 0 and CHIR was removed after 24 h incubation. IWP4 (5 μM) were added on day 3 and removed after 48 h incubation. The cultures were maintained in RPMI with B27 (no insulin) until day 7 and switched to the RPMI with B27 for the rest of the culture time. CMs were harvested by incubating cells with 10× trypLE for 15–30 min at 37°C.

### Primary cultures

GFP-expressing HUVECs were grown and cultured in endothelial cell growth medium (EGM2). Human cardiac fibroblasts (cFBs) were cultured using FGM3. DPSCs were cultured in low-glucose DMEM (1 g/L) supplemented with 10% FBS, 1% pen-strep (100 U/mL), 1% GlutaMAX (100×) supplement, and 1% MEM non-essential amino acids solution (100×). All cells were cultured and passaged according to the manufacturer's protocol. All primary cells were used before reaching passage 10.

### Animal models

Eight adult athymic *rnu/rnu* rats (four male and four female, aged 7–8 weeks, weighing 180–200 g) were obtained from Charles River Laboratories. Rats were housed under standard conditions (including controlled temperature, humidity, and a 12-h light/dark cycle) with free access to food and water. Animals were randomly allocated to experimental groups, ensuring that each group contained an equal number of males and females. All procedures, including induction of anesthesia with isoflurane for surgical interventions, were performed following institutional and national guidelines, adhering to ARRIVE recommendations for the care and use of laboratory animals.

### PDMS mold fabrication

PDMS molds for the culture of microtissues were fabricated using soft lithography. Features of varying shapes, sizes, and pillars were designed in AutoCAD and fabricated onto a silicon wafer using MicroWriter ML3 Pro (maskless lithography). Briefly, a thin layer of SU-8 25 was spun onto a 4-in silicon wafer at 3,000 rpm for 30 s, prebaked, and exposed to establish the seed layer. A second layer of SU-8 2150 was then spun onto the wafer at 1,500 rpm for 30 s for an expected thickness of 300 μm. The pattern was directly projected onto the surface by the ML3 MicroWriter with a resist sensitivity of 400 mJ/cm$^2$. PDMS was cast onto the developed SU-8 master at a 10:1 polymer:curing agent ratio and cured overnight at 75°C under vacuum. The PDMS molds were then cut, peeled, and autoclaved for sterilization.

### Generation of microtissues

Sterilized PDMS molds were pre-soaked in 5% pluronic F-127 in PBS, centrifuged for 5 min at 2,000 × *g* to ensure complete surface wetting, and then placed inside a 12-well plate.

GFP-tagged HUVECs and DPSCs were combined at a ratio of 5:1 and centrifuged at 300 × *g* for 5 min. The resulting pellet was resuspended in EGM2 medium at a concentration of 10 million cells/mL. Each construct was seeded with 50 μL of the cell suspension, allowing the cells to settle into the mold features for approximately 30 min. Any remaining cell/media suspension on top of the construct was carefully removed. EGM2 media was slowly added to each well. The cultures were maintained at 37°C and 5% CO$_2$. Vascular tissues were harvested by pipetting at day 7 and evaluated for viability by live/dead staining by CFDA (Thermo Fisher, C2925) and PI (Life Technologies P3566).

CM and cFBs were combined at a 10:1 ratio and centrifuged at 300 × *g* for 5 min. The resulting pellet was resuspended in induction 3 medium (I3M) at a concentration of 10 million cells/mL. A minimum of three replicates were used for *in vitro* experiments. Each construct was seeded with 50 μL of the cell suspension, allowing the cells to settle into the mold features for approximately 30 min. Any remaining cell/media suspension on top of the construct was carefully removed. We aimed to seed 4,000 cells/well. At day 7 post-seeding, DNA of microtissues was isolated and evaluated using PicoGreen dsDNA Assay Kit (Invitrogen P11496), confirming 2,223 ± 72 cells present in each microtissue at this time point. I3M, comprised of StemPro-34 complete media supplemented with 20 mM HEPES, 1% GlutaMAX, and 213 μg/mL 2-phosphate ascorbic acid, was then slowly added to the wells. The cultures were maintained at 37°C and 5% CO$_2$.

VE-cadherin and cardiac TnT immunostaining was performed on day 7 to evaluate microtissue cellular morphology.

*Measuring microtissues formation success rate*. Successful microtissue formation was quantified using bright-field images of a 10.6 × 10.6 mm section. Microwells containing tissues that compacted according to the specific shape and formed around the features/pillars were counted as successful. In contrast, microwells containing tissues that were detached from the pillars or only compacted around one pillar were considered unsuccessful. Success rate was defined as the number of intact tissues anchored to the pillars divided by the total number of tissues seeded in the experiment. Three replicates (images of three different seedings) were used for the analysis, with at least 30 tissues counted per mold/image, from $n = 3$ different batches of seeding.

*Quantification of vascular microtissue dimensions*. The dimensions of the seeded microtissues were quantified using ImageJ. Tissue dimensions were measured 1 day following pillar seeding. $n = 3$ replicates (images of 3 different microtissues seeded within their respective molds) were used. At least 3 tissues were counted for each mold/replicate. Width was defined as the long axis of the shape, whereas length was defined as the short axis of the shape.

*Quantification of cardiac microtissue sarcomere alignment*. Sarcomere alignment of cardiac microtissues was analyzed using the ImageJ plugin Directionality. Analysis was carried out with 180 bins from −90° to +90° using the Fourier components method. Cardiac microtissues were fixed and stained for TnT 7 days after seeding. Confocal images of at least 3 different microtissues were used for each shape. The z-series of each tissue was projected into a single 2D image using Z Project. The resulting data was plotted in a circular histogram with MATLAB. Furthermore, coherency (percent of structures along a computed dominant direction) was analyzed using a separate ImageJ plugin, OrientationJ.

*Establishment of calibration curves*. The calibration curve to measure the force required to displace pillars were generated out using a microscale mechanical tester, Microtester MT-LT (CellScale, Ontario, Canada). A 0.2032 mm diameter circular tungsten microbeam was used to displace the pillar head. Before the test, the platform was placed on the testing stage and secured with tape. The probe tip was placed adjacent to the pillar head without contact and gradually moved toward the center of the platform at a velocity of 4 μm/s. The tip displaced the pillar head and applied force perpendicular to the original pillar position (Figure 2S).

*Force quantification*. Bright-field videos of contracting tissues were taken using an Olympus IX81 microscope at 4× magnification. A 100 × 100 px section around each pillar was cropped and used for analysis. Images were first processed using the Gaussian blur and minimum filter. Pillar deflection was then tracked using an ImageJ plugin, SpotTracker. Contractile dynamics of the microtissues were then analyzed with a custom MATLAB code. A minimum of 3 microtissues were analyzed per shape.

### *3D fibrin hydrogel seeding*

Cardiac microtissues were incorporated with ECs and DPSCs (microtissue/EC/DPSC) at a cell ratio of 2:1:1 in 20 mg/mL fibrinogen for vascularized cardiac tissue seeding. The number of cells in the microtissues was quantified with PicoGreen dsDNA Assay Kits (Invitrogen) according to the published protocol. To prepare fibrin hydrogel with cells and microtissues, 7 μL of the cell/microtissue/fibrin mixture was mixed with 2 μL of thrombin (25 U/mL) and placed as a dome on a polystyrene surface. The dispersed CM:EC:DPSC co-culture (ratio of 2:1:1) was used as the control. A microtissue-only group with a consistent CM quantity was prepared as the appropriate control. The formation of vascular networks and tissue contractility were monitored by fluorescence microscopy between days 0 and 14. Vessel network evaluation was performed with AngioTool (NIH).

For *in vivo* experiments, four groups were prepared with 20 mg/mL fibrinogen for vascularized cardiac tissue seeding. Cellular composition was as follows:

(1) cardiac microtissues incorporated with ECs and DPSCs (microtissue/EC/DPSC) at a cell number ratio of 2:1:1;
(2) cardiac microtissues only with the same CMs as group 1;
(3) CM:EC:DPSC co-culture using dispersed CMs incorporated with ECs and DPSCs (CM:EC:DPSC) at a cell number ratio of 2:1:1; and
(4) dispersed CMs with the same number of CMs as previous groups.

Briefly, 18 μL of the cell/microtissue/fibrin mixture was mixed with 3 μL of thrombin (25 U/mL) and placed as a dome on a polystyrene surface. EGM2 was added and the fibrin dome was carefully released from the polystyrene surface with a cell scraper immediately prior to omental transplantation.

### *Evaluation of fibrin dome vascular morphology*

Fibrin domes were observed under the fluorescent microscope (Olympus IX81) weekly and images taken to evaluate vasculature formation within the tissues. The location and morphology of GFP-tagged HUVECs were monitored to serially evaluate vasculature dynamics. After 2 weeks of culture, tissues were stained for VE-cadherin (CD144) and α-actinin to assess both vascular networks and CM morphology within the constructs. Vessel morphology parameters including average vessel length, vessel density, total number of junctions, junctions per vessel area, and lacunarity (a measurement of how fractal features fill in the space), were quantified using AngioTool (NIH) on GFP channel images. A greater length of vessels and a higher count of vessel junctions with low lacunarity were interpreted as signs of a more advanced and intricate vascular network.

### *Immunohistochemical (IHC) staining and confocal imaging*

At the appropriate endpoint, tissues were fixed overnight at 4°C in 4% paraformaldehyde (PFA), permeabilized, and blocked using 10% FBS in PBS with 0.1% Triton X-100 for 1 h before adding primary antibodies. All antibody incubation was performed at 4°C. Samples were incubated with rabbit anti-CD144 (Abcam 33168), mouse anti-α-actinin (Abcam 137346), and rabbit anti-MLC2v (Abcam 79935), for 48 h, followed by 24 h of washing in PBS solution and 48 h of secondary antibody incubation. Goat anti-rabbit Texas Red (Thermo Scientific A32795) and goat anti-mouse Alexa Fluor 647 (Thermo Scientific A-21240) were used as secondary antibodies. All tissues were counterstained with DAPI. Tissues were imaged with a Leica light-sheet confocal microscope or Nikon A1R microscope at 10× and 20× magnifications.

### *LDH assay*

LDH release was measured for the two groups cultivated in fibrin hydrogel (CM/EC/DPSC and microtissue/EC/DPSC) from media samples collected at day 10 of culture, with the last media change 2 days prior to media collection. LDH was quantified using an LDH cytotoxicity assay kit (Cayman) according to the manufacturer's instructions.

### *Quantification of circulating cell-free mtDNA*

mtDNA was extracted from conditioned media of two groups cultivated in fibrin hydrogel: CM/EC/DPSC and microtissue/EC/DPSC. Samples (100 μL) were collected on day 10, with the last media change 2 days prior to media collection. The QIAamp DNA Mini Kit (Qiagen) was used for extraction, and DNA was eluted with 100 μL of ultra-pure distilled water (Invitrogen). A synthesized PCR product oligonucleotide (Integrated DNA Technologies) was diluted to create a concentration range from $10^8$ to $10^2$ copies/μL to estimate the absolute concentration of cell-free circulating mtDNA (ccf-mtDNA). The mitochondrial genes ND4 and ND1 were chosen to represent the major and minor arcs of the mitochondrial genome. A TaqMan Duplex PCR assay was conducted using Bio-Rad's C1000 Thermal Cycler CFX96 Real-Time System. The 20 μL reaction mixture included 10 μL of TaqMan Fast Advanced Master Mix (Thermo Fisher), 4 μL of DNA, 1 μL each of forward and reverse primers, and 1 μL of TaqMan probe for each gene. The qPCR conditions were as follows: 50°C for 2 min, 95°C for 20 s, followed by 40 cycles of 95°C for 3 s and 60°C for 30 s, with a fluorescent read at each cycle.

Primer/probe sequence

ND4-F1 5′-CCATTCTCCTCCTATCCCTCAAC-3′

ND4-R1 5′-ACAATCTGATGTTTTGGTTAAACTATATTT-3′

ND4-Probe 5′-FAM/CCGACATCA/ZEN/TTACCGGGTTTTCCTCTTG/3IABkFQ/-3′

ND1-F1 5′-CCCTAAAACCCGCCACATCT-3′

ND1-R1 5′-GAGCGATGGTGAGAGCTAAGGT-3′

ND1-Probe 5′-HEX/CCATCACCC/ZEN/TCTACATCACCGCCC/3IABkFQ/-3′

ND4 + ND1 geneblock - 5′-CACGAGAAAACACCCTCATGTTCATACACCTATCCCCCATTCTCCTCCTATCCCTCAACCCCGACATCATTACCGGGTTTTCCTCTTGTAAATATAGTTTAACCAAAACATCAGATTGTGAATCTGACAACAGAGGCTCTCTTCACCAAAGAGCCCCTAAAACCCGCCACATCTACCATCACCCTCTACATCACCGCCCCGACCTTAGCTCTCACCATCGCTCTTCTACTATGAACCCCCCTCCCCATACCCAA-3′

### *Secretomics analysis*

Phenol red-free conditioned media was collected from three pooled fibrin domes containing either CMs/ECs/DPSCs or microtissues/ECs/DPSCs on day 10 of culture. The media was centrifuged at 2,500 × *g* for 20 min at 4°C to remove cell debris. The supernatant was concentrated 10-fold using a 3 kDa MWCO Amicon centrifuge filtration column (Millipore) at 4,000 × *g* for 1 h at 4°C and then dried using a SpeedVac (Thermo Fisher Scientific) for 2 h at medium heat. 20 μg of conditioned media-derived proteins from each sample were denatured and reduced with 8 M urea, 10 mM DTT, and 100 mM Tris-HCl (pH 8.5) at 60°C for 30 min, followed by alkylation with 100 mM iodoacetamide for 15 min. Alkylation was quenched with DTT to a final concentration of 40 mM, and urea was diluted to less than 1 M with 50 mM ammonium bicarbonate. Proteins were digested with 0.2 μg of trypsin (Sigma-Aldrich) overnight at 37°C. The resulting peptides were acidified and desalted using in-house C18 pipette tips. Analysis was performed on an Easy nLC-1200 coupled to a Thermo Q Exactive HF mass spectrometer in top 20 data-dependent acquisition mode. Peptides were separated on a PepMap RSLC C18 (2 μm, 75 μm × 50 cm) column and a PepMap 100 C18 (3 μm, 75 μm × 2 cm) precolumn with a 120-min gradient from 5% to 40% buffer B (0.1% formic acid in 80% acetonitrile). Data were analyzed using MaxQuant (v1.6.10.43) with specific tryptic peptides detected at a false discovery rate (FDR) of 0.01 and label-free quantification (LFQ) performed with default parameters. Identified and quantified protein groups were pillar-processed in Perseus (v1.6.5.0)[119] and the Cytoscape StringApp.[120]

The mass spectrometry proteomics data have been deposited to the ProteomeXchange Consortium (http://proteomecentral.proteomexchange.org) via the PRIDE partner repository[117] with the dataset identifier PRIDE: PXD055832.

### Cytokine array

Media was collected from 3 pooled fibrin domes containing either CMs/ECs/DPSCs or microtissues/ECs/DPSCs at day 14 of culture using the Raybiotech Human L507 Array Glass Slide to compare cytokine levels. In a separate experiment, media was collected from three pooled fibrin domes containing microtissues/ECs/DPSCs or microtissues only on day 14 of culture using the Raybiotech Human L507 Array Glass Slide to compare cytokine levels. Cytokine secretion measurements were performed according to the manufacturer's instructions. Slides were stored in a light-tight box prior to scanning using the Axon 4200A microarray scanner (Molecular Devices, Sunnyvale, CA). Photomultiplier tube (PMT) gain was manually adjusted to 370 and scanning power to 55% to sufficiently illuminate all positive control quadruplicate spots in the absence of fluorescence saturation using a 532 nm excitation laser. Then, all slides were scanned at high resolution (10 μm). Gene array list (GAL) visual analysis masks were automatically overlayed onto the scanned images and manually adjusted at each spot using the GenePix Pro software version 6.1.0.2 (Molecular Devices, Sunnyvale, CA). Fluorescence quantification at the masked spots and subsequent image optimization was automatically performed using GenePix Pro. The median fluorescence intensity observed following excitation at 532 nm was corrected for the local background signal at each spot to yield a corrected median fluorescence intensity (cMFI). Volcano plots and statistical tests were done using Prism software, and a heatmap of significant cytokines was generated using Morpheus (https://software.broadinstitute.org/morpheus).

### Large tissue formation in perfusable tissue chamber

The platform was assembled from three separate components: (1) micro-milled, bottomless, interconnected wells (inner dimension 10 × 10 × 30 mm) with sockets for placing electrodes; (2) elastic tubes with side microholes (diameter of 0.5 mm) for tissue attachment, tissue force sensing, and liquid perfusion; and (3) a glass bottom (50 × 75 × 1 mm). The three components were assembled and fixed by PDMS glue. Bottomless culture wells and the molds to produce elastic tubes were fabricated out of polysulfone using a computer numerical control (CNC) milling machine with mating features for stability and repeatable positioning.

The elastic tubes were formed by centrifugal casting of PDMS (Dow Corning Sylgard 184) through the polysulfone molds with an embedded needle. The needle was first inserted into polysulfone molds fabricated by CNC machining and PDMS (10:1 ratio of base:curing agent) was centrifugally cast at 400 relative centrifugal force for 5 min and cured in an oven at 60°C for 1 h. The resulting component consisted of 30 elastic tubes to support the formation of 15 tissues. The tubes were 1 mm in diameter, 9 mm in length, and spaced 6 mm axis-to-axis.

Cardiac microtissues were incorporated with ECs and DPSCs (CM:DPSC:EC ratio of 2:1:1) in 20 mg/mL fibrinogen for vascularized cardiac tissue seeding. Briefly, 200 μL of the cell/microtissue/fibrin mixture was mixed with 50 μL of thrombin (25 U/mL) and placed as a dome on a polystyrene surface. The CM/EC/DPSC co-culture (CM:DPSC:EC ratio of 2:1:1) was used as the control. Tissues were retrieved from culture 3 days following pillar seeding. The tissue formation and contractility were monitored on day 7.

### Omental implantation

Adult male (*n* = 4) and female (*n* = 4) athymic *rnu/rnu* rats (age 7–8 weeks, Charles River Laboratories) weighing 180–200 g were used. Following induction of anesthesia with isoflurane, a 2–3 cm midline laparotomy was made and the greater omentum identified and externalized from the peritoneal cavity. Four fibrin hydrogels containing either dispersed CMs, dispersed CMs/ECs/DPSCs, microtissues, or microtissues/ECs/DPSCs were placed on the omentum and wrapped within omental fat using 7-0 Prolene suture. Fibrin domes containing dispersed cells consisted of 1.2 × $10^5$ CMs (if CMs/ECs/DPSCs, cells were incorporated at a ratio of 2:1:1) in a total hydrogel volume of 30 μL. Those containing microtissues consisted of 2.4 × $10^5$ CMs (if microtissues/ECs/DPSCs, cells were incorporated at a ratio of 4:1:1) in a total hydrogel volume of 30 μL, with 40–60 microtissues initially seeded into each fibrin dome. Titanium microclips (GEM MicroClip, Synovis Micro Companies Alliance) were placed on the omental fat surrounding each scaffold using a pre-determined identification system to ensure experimental groups could be differentiated appropriately upon sample explantation. The omentum was then returned to the abdominal cavity and the laparotomy closed in standard fashion using running 5-0 vicryl for the abdominal wall musculature and skin staples in interrupted fashion to approximate the overlying skin. 1 week following implantation, rats were euthanized and the omental samples removed for contractility assessment and histological/IHC studies by gently dissecting each sample from the surrounding fat.

### *Contractility assessment following surgical explantation*

Immediately following surgical explantation, omental tissues were transferred to an electrical stimulation chamber and positioned between the carbon rods. 4× bright-field movies were taken of spontaneous cardiac tissue beating and beating under stimulation at 1 Hz. The minimum voltage per cm required to stimulate the synchronized contraction of the tissue (ET) and the maximum frequency the tissue could achieve in response to the stimulation pulse at twice the ET (MCR) were measured and recorded. Thus, a lower ET and higher MCR implied a more electrically responsive tissue. If the omental tissues could not be excited by an electric field strength of up to 24 V/cm, they were deemed as non-beating.

### *Histology and immunohistochemistry for* in vivo *samples*

Following assessment of functional properties, omental tissues were placed within a 10% neutral buffered formalin solution overnight and then stored in 70% ethanol at 4°C. Samples were embedded in paraffin, sectioned serially (5 μm thickness), and stained with H&E. For IF staining, cut sections were deparaffinized and rehydrated prior to heat-mediated antigen retrieval in citrate buffer for 25 min. Following blocking with protein block (Agilent Dako) to reduce nonspecific background staining, sections were incubated overnight with antibodies for TnT (Thermo Fischer Scientific MA5-12960, 1:200), CD68 (Abcam ab125212, 1:500), CD206 (Abcam ab64693, 1:1,000), or YAP1 (Thermo Fischer Scientific PA1-46189, 1:200). Primary antibody binding was visualized using species-specific Alexa Fluor 488 or 647-conjugated secondary antibodies (Thermo Fischer Scientific). Sections were counterstained with DAPI (1:1,000, Thermo Fischer Scientific) and mounted using Fluorescence Mounting Medium (Agilent Dako). For immunohistochemical staining, slides were deparaffinized and heat-mediated antigen retrieval performed in the same manner. Endogenous peroxidase activity was quenched via incubation with 3% hydrogen peroxide. Following blocking with 2.5% normal horse serum, sections were incubated overnight with primary antibodies for CD31 (Dako M0823, 1:300 with cross-reactivity to human ECs only; Novus NB-100-2284, 1:300 with cross-reactivity to both human and rat ECs). Slides were developed using the ImmPRESS HRP Horse Anti-Rabbit IgG Polymer Detection Kit (Vector Laboratories MP-7401) following the manufacturer's protocol, followed by color development with DAB (Dako). Sections were counterstained with hematoxylin and mounted using MM 23 mounting media (Leica).

Fluorescence images were digitally acquired with a Zeiss AxioObserver microscope attached to a Hamamatsu ORCA-Flash 4.0 camera under a 20× magnification objective or using a Zeiss AxioScan fluorescence scanner at 40× magnification. Bright-field images were acquired using the Aperio AT2 bright-field scanner (Leica Biosystems) at 20× magnification. Image analysis was performed using ImageJ.

## Quantification and statistical analysis

Statistical analysis was performed using Prism version 10.0, using one-way, two-way, or repeated measures ANOVA or a t test, as appropriate based on the dataset. Normality and equality of variance was tested. Pairwise multiple comparison procedures (Tukey's post hoc method or Holm-Sidak method) were used for one-way ANOVA and two-way ANOVA tests. $p < 0.05$ was considered significant for all statistical tests.

All *in vivo* data are represented as mean ± standard deviation (SD). Indicated sample sizes ($n$) represent individual omental tissue samples (ET/MCR) or tissue sections (IHC/IF). Differences between experimental groups were analyzed by ordinary one-way ANOVA, with the Tukey test used for pairwise multiple comparisons. $p < 0.05$ was considered statistically significant.

## RESOURCE AVAILABILITY

### Lead contact

Further information and requests for resources and reagents should be directed to and will be fulfilled by the lead contact, Milica Radisic (m.radisic@utoronto.ca).

### Materials availability

This study did not generate new unique reagents.

### Data and code availability

- The mass spectrometry proteomics data have been deposited to the ProteomeXchange Consortium (http://proteomecentral.proteomexchange.org) via the PRIDE partner repository with the dataset identifier PRIDE: PXD055832 and are publicly available as of the date of publication, accession numbers are listed in the key resources table.
- All data is published at Mendeley Data Repository and can be accessed through the following DOIs:

Dataset #1 DOI: https://doi.org/10.17632/cvcw2x6zxb.1.
Dataset #2 DOI: https://doi.org/10.17632/k34yrsj9pp.1.
Dataset #3 DOI: https://doi.org/10.17632/25w8vxsm62.1.
Dataset #4 DOI: https://doi.org/10.17632/7g7yhp9gpd.1.

- Other materials and resources are listed in the key resources table.

## ACKNOWLEDGMENTS

This work was funded by the National Institutes of Health grant (2R01 HL076485), Natural Sciences and Engineering Research Council of Canada (NSERC) Discovery Grant (RGPIN 326982-10), NSERC Strategic Grant (STPGP 506689-17), Canadian Institutes of Health Research (CIHR) Foundation Grant (FDN-167274), Canada Foundation for Innovation/Ontario Research Fund grant (36442) and Additional Ventures Single Ventricle Research Fund project (1289463). M.R. was supported by Canada Research Chairs and Killam Fellowship. S.L. was supported by the Rothschild and European Molecular Biology Organization (EMBO) (ALTF 530-2022) Fellowships. C.L.C was supported by Heart and Stroke Foundation of Canada grant (G-22-0032216). S. A.S. was supported by a PRiME fellowship. Y.Z. was supported by CIHR and Stem Cell Network PDF Fellowship. R.K. is supported by a CIHR postdoctoral fellowship. G.V.-N. is supported by NIH (P41 EB027062 and 5R01HL076485), NSF (NSF1647837). The authors would like to thank Dr. Holger Gerhard for helpful discussions on YAP signaling and Dr. Stephen Juvet for the use of microarray scanner.

## AUTHOR CONTRIBUTIONS

Conceptualization, Y.Z, and M.R.; methodology, Y.Z., R.K., and K.C.; investigation, Y.Z., R.K., K.C., Y.W., Q.W., R.X.Z.L., K.W., S.A.S., D.V., and E.L.B.; formal analysis, S.L., writing – original draft, Y.Z., R.K., and K.C.; writing – review & editing, Y.Z., R.K., G.V.-N. and M.R.; funding acquisition, G.V.-N. and M.R.; resources, S.O., D.F.B., K.Y., C.L.C., A.C.A., G.V.-N. and M.R.; supervision, G.V.-N. and M.R.

## DECLARATION OF INTERESTS

M.R. and Y.Z. are inventors on an issued patent that describes Biowire technology. This patent is licensed to Valo Health. M.R. and Y.Z. receive licensing revenue. G.V.-N. reports inventorship on patents for cardiac tissue engineering.

## SUPPLEMENTAL INFORMATION

Supplemental information can be found online at https://doi.org/10.1016/j.celbio.2025.100075.

Received: September 27, 2024
Revised: February 14, 2025
Accepted: April 2, 2025
Published: April 29, 2025

## REFERENCES

1. Silver, S.E., Barrs, R.W., and Mei, Y. (2021). Transplantation of Human Pluripotent Stem Cell-Derived Cardiomyocytes for Cardiac Regenerative Therapy. Front. Cardiovasc. Med. *8*, 707890. https://doi.org/10.3389/fcvm.2021.707890.
2. Kieda, J., Shakeri, A., Landau, S., Wang, E.Y., Zhao, Y., Lai, B.F., Okhovatian, S., Wang, Y., Jiang, R., and Radisic, M. (2024). Advances in cardiac tissue engineering and heart-on-a-chip. J. Biomed. Mater. Res. A *112*, 492–511. https://doi.org/10.1002/jbm.a.37633.
3. Sun, X., Wu, J., Qiang, B., Romagnuolo, R., Gagliardi, M., Keller, G., Laflamme, M.A., Li, R.K., and Nunes, S.S. (2020). Transplanted microvessels improve pluripotent stem cell-derived cardiomyocyte engraftment and cardiac function after infarction in rats. Sci. Transl. Med. *12*, eaax2992. https://doi.org/10.1126/scitranslmed.aax2992.
4. Zhao, Y., Wang, E.Y., Lai, F.B.L., Cheung, K., and Radisic, M. (2023). Organs-on-a-chip: a union of tissue engineering and microfabrication. Trends Biotechnol. *41*, 410–424. https://doi.org/10.1016/j.tibtech.2022.12.018.
5. Bannerman, A.D., Ze Lu, R.X., Korolj, A., Kim, L.H., and Radisic, M. (2018). The use of microfabrication technology to address the challenges of building physiologically relevant vasculature. Curr. Opin. Biomed. Eng. *6*, 8–16. https://doi.org/10.1016/j.cobme.2017.12.003.
6. Zimmermann, W.H. (2017). Remuscularization of the failing heart. J. Physiol. *595*, 3685–3690. https://doi.org/10.1113/JP273098.
7. Luzuriaga, J., Irurzun, J., Irastorza, I., Unda, F., Ibarretxe, G., and Pineda, J.R. (2020). Vasculogenesis from Human Dental Pulp Stem Cells Grown in Matrigel with Fully Defined Serum-Free Culture Media. Biomedicines *8*, 483. https://doi.org/10.3390/biomedicines8110483.
8. Hilkens, P., Fanton, Y., Martens, W., Gervois, P., Struys, T., Politis, C., Lambrichts, I., and Bronckaers, A. (2014). Pro-angiogenic impact of dental stem cells in vitro and in vivo. Stem Cell Res. *12*, 778–790. https://doi.org/10.1016/j.scr.2014.03.008.
9. Bronckaers, A., Hilkens, P., Fanton, Y., Struys, T., Gervois, P., Politis, C., Martens, W., and Lambrichts, I. (2013). Angiogenic properties of human dental pulp stem cells. PLoS One *8*, e71104. https://doi.org/10.1371/journal.pone.0071104.
10. Guo, S., Redenski, I., Landau, S., Szklanny, A., Merdler, U., and Levenberg, S. (2020). Prevascularized Scaffolds Bearing Human Dental Pulp Stem Cells for Treating Complete Spinal Cord Injury. Adv. Healthc. Mater. *9*, e2000974. https://doi.org/10.1002/adhm.202000974.
11. Debbi, L., Zohar, B., Shuhmaher, M., Shandalov, Y., Goldfracht, I., and Levenberg, S. (2022). Integrating engineered macro vessels with self-assembled capillaries in 3D implantable tissue for promoting vascular integration in-vivo. Biomaterials *280*, 121286. https://doi.org/10.1016/j.biomaterials.2021.121286.
12. Tulloch, N.L., Muskheli, V., Razumova, M.V., Korte, F.S., Regnier, M., Hauch, K.D., Pabon, L., Reinecke, H., and Murry, C.E. (2011). Growth of engineered human myocardium with mechanical loading and vascular coculture. Circ. Res. *109*, 47–59. https://doi.org/10.1161/CIRCRESAHA.110.237206.
13. Zhang, B., Montgomery, M., Chamberlain, M.D., Ogawa, S., Korolj, A., Pahnke, A., Wells, L.A., Massé, S., Kim, J., Reis, L., et al. (2016). Biodegradable scaffold with built-in vasculature for organ-on-a-chip engineering and direct surgical anastomosis. Nat. Mater. *15*, 669–678. https://doi.org/10.1038/nmat4570.
14. Lai, B.F.L., Davenport Huyer, L., Lu, R.X.Z., Drecun, S., Radisic, M., and Zhang, B. (2017). VADE: integrated vasculature for assessing dynamic events. Adv. Funct. Mater. *27*, 1703524.
15. O'Connor, C., Brady, E., Zheng, Y., Moore, E., and Stevens, K.R. (2022). Engineering the multiscale complexity of vascular networks. Nat. Rev. Mater. *7*, 702–716. https://doi.org/10.1038/s41578-022-00447-8.
16. Lai, B.F.L., Davenport Huyer, D., Lu, R.X.Z., Drecun, S., Radisic, M., and Zhang, B. (2017). VADE: Integrated Vasculature for Assessing Dynamic Events. Adv. Funct. Mater. *27*, 1703524.
17. Grigoryan, B., Paulsen, S.J., Corbett, D.C., Sazer, D.W., Fortin, C.L., Zaita, A.J., Greenfield, P.T., Calafat, N.J., Gounley, J.P., Ta, A.H., et al. (2019). Multivascular networks and functional intravascular topologies within biocompatible hydrogels. Science *364*, 458–464. https://doi.org/10.1126/science.aav9750.
18. Noor, N., Shapira, A., Edri, R., Gal, I., Wertheim, L., and Dvir, T. (2019). 3D Printing of Personalized Thick and Perfusable Cardiac Patches and Hearts. Adv. Sci. (Weinh) *6*, 1900344. https://doi.org/10.1002/advs.201900344.
19. Silberman, E., Oved, H., Namestnikov, M., Shapira, A., and Dvir, T. (2023). Post-Maturation Reinforcement of 3D-Printed Vascularized Cardiac Tissues. Adv. Mater. *35*, e2302229. https://doi.org/10.1002/adma.202302229.
20. Skylar-Scott, M.A., Uzel, S.G.M., Nam, L.L., Ahrens, J.H., Truby, R.L., Damaraju, S., and Lewis, J.A. (2019). Biomanufacturing of organ-specific tissues with high cellular density and embedded vascular channels. Sci. Adv. *5*, eaaw2459. https://doi.org/10.1126/sciadv.aaw2459.
21. Okhovatian, S., Khosravi, R., Wang, E.Y., Zhao, Y., and Radisic, M. (2024). Biofabrication strategies for cardiac tissue engineering. Curr. Opin. Biotechnol. *88*, 103166. https://doi.org/10.1016/j.copbio.2024.103166.
22. Miri, A.K., Khalilpour, A., Cecen, B., Maharjan, S., Shin, S.R., and Khademhosseini, A. (2019). Multiscale bioprinting of vascularized models. Biomaterials *198*, 204–216. https://doi.org/10.1016/j.biomaterials.2018.08.006.
23. Romagnuolo, R., Masoudpour, H., Porta-Sánchez, A., Qiang, B., Barry, J., Laskary, A., Qi, X., Massé, S., Magtibay, K., Kawajiri, H., et al. (2019). Human Embryonic Stem Cell-Derived Cardiomyocytes Regenerate the Infarcted Pig Heart but Induce Ventricular Tachyarrhythmias. Stem Cell Rep. *12*, 967–981. https://doi.org/10.1016/j.stemcr.2019.04.005.
24. Tachibana, A., Santoso, M.R., Mahmoudi, M., Shukla, P., Wang, L., Bennett, M., Goldstone, A.B., Wang, M., Fukushi, M., Ebert, A.D., et al. (2017). Paracrine Effects of the Pluripotent Stem Cell-Derived Cardiac Myocytes Salvage the Injured Myocardium. Circ. Res. *121*, e22–e36. https://doi.org/10.1161/CIRCRESAHA.117.310803.
25. Gruh, I., Martens, A., Cebotari, S., Schrod, A., Haase, A., Halloin, C., Triebert, W., Goecke, T., Arar, M., Hoeffler, K., et al. (2024). Cell therapy with human iPSC-derived cardiomyocyte aggregates leads to efficient engraftment and functional recovery after myocardial infarction in non-human primates. Preprint at bioRxiv. https://doi.org/10.1101/2023.12.31.573775.
26. Sun, X., Altalhi, W., and Nunes, S.S. (2016). Vascularization strategies of engineered tissues and their application in cardiac regeneration. Adv.

Drug Deliv. Rev. *96*, 183–194. https://doi.org/10.1016/j.addr.2015.06.001.

27. Ruan, J.L., Tulloch, N.L., Razumova, M.V., Saiget, M., Muskheli, V., Pabon, L., Reinecke, H., Regnier, M., and Murry, C.E. (2016). Mechanical Stress Conditioning and Electrical Stimulation Promote Contractility and Force Maturation of Induced Pluripotent Stem Cell-Derived Human Cardiac Tissue. Circulation *134*, 1557–1567. https://doi.org/10.1161/CIRCULATIONAHA.114.014998.
28. Zhao, Y., Rafatian, N., Feric, N.T., Cox, B.J., Aschar-Sobbi, R., Wang, E. Y., Aggarwal, P., Zhang, B., Conant, G., Ronaldson-Bouchard, K., et al. (2019). A Platform for Generation of Chamber-Specific Cardiac Tissues and Disease Modeling. Cell *176*, 913–927.e18. https://doi.org/10.1016/j.cell.2018.11.042.
29. Landau, S., Zhao, Y., Hamidzada, H., Kent, G.M., Okhovatian, S., Lu, R. X.Z., Liu, C., Wagner, K.T., Cheung, K., Shawky, S.A., et al. (2024). Primitive macrophages enable long-term vascularization of human heart-on-a-chip platforms. Cell Stem Cell *31*, 1222–1238.e10. https://doi.org/10.1016/j.stem.2024.05.011.
30. Landau, S., Ben-Shaul, S., and Levenberg, S. (2018). Oscillatory Strain Promotes Vessel Stabilization and Alignment through Fibroblast YAP-Mediated Mechanosensitivity. Adv. Sci. (Weinh) *5*, 1800506. https://doi.org/10.1002/advs.201800506.
31. Di Nicola, V. (2019). Omentum a powerful biological source in regenerative surgery. Regen. Ther. *11*, 182–191. https://doi.org/10.1016/j.reth.2019.07.008.
32. Boogerd, C.J., Perini, I., Kyriakopoulou, E., Han, S.J., La, P., van der Swaan, B., Berkhout, J.B., Versteeg, D., Monshouwer-Kloots, J., and van Rooij, E. (2023). Cardiomyocyte proliferation is suppressed by ARID1A-mediated YAP inhibition during cardiac maturation. Nat. Commun. *14*, 4716. https://doi.org/10.1038/s41467-023-40203-2.
33. Wang, J., Liu, S., Heallen, T., and Martin, J.F. (2018). The Hippo pathway in the heart: pivotal roles in development, disease, and regeneration. Nat. Rev. Cardiol. *15*, 672–684. https://doi.org/10.1038/s41569-018-0063-3.
34. Mia, M.M., Cibi, D.M., Abdul Ghani, S.A.B., Song, W., Tee, N., Ghosh, S., Mao, J., Olson, E.N., and Singh, M.K. (2020). YAP/TAZ deficiency reprograms macrophage phenotype and improves infarct healing and cardiac function after myocardial infarction. PLoS Biol. *18*, e3000941. https://doi.org/10.1371/journal.pbio.3000941.
35. Kemp, M., Donovan, J., Higham, H., and Hooper, J. (2004). Biochemical markers of myocardial injury. Br. J. Anaesth. *93*, 63–73. https://doi.org/10.1093/bja/aeh148.
36. Lu, R.X.Z., Rafatian, N., Zhao, Y., Wagner, K.T., Beroncal, E.L., Li, B., Lee, C., Chen, J., Churcher, E., Vosoughi, D., et al. (2024). Cardiac tissue model of immune-induced dysfunction reveals the role of free mitochondrial DNA and the therapeutic effects of exosomes. Sci. Adv. *10*, eadk0164. https://doi.org/10.1126/sciadv.adk0164.
37. Bertheloot, D., Latz, E., and Franklin, B.S. (2021). Necroptosis, pyroptosis and apoptosis: an intricate game of cell death. Cell. Mol. Immunol. *18*, 1106–1121. https://doi.org/10.1038/s41423-020-00630-3.
38. Odorisio, T., Schietroma, C., Zaccaria, M.L., Cianfarani, F., Tiveron, C., Tatangelo, L., Failla, C.M., and Zambruno, G. (2002). Mice overexpressing placenta growth factor exhibit increased vascularization and vessel permeability. J. Cell Sci. *115*, 2559–2567. https://doi.org/10.1242/jcs.115.12.2559.
39. Balta, S., Mikhailidis, D.P., Demirkol, S., Ozturk, C., Celik, T., and Iyisoy, A. (2015). Endocan: A novel inflammatory indicator in cardiovascular disease? Atherosclerosis *243*, 339–343. https://doi.org/10.1016/j.atherosclerosis.2015.09.030.
40. Scholz, A., Plate, K.H., and Reiss, Y. (2015). Angiopoietin-2: a multifaceted cytokine that functions in both angiogenesis and inflammation. Ann. N. Y. Acad. Sci. *1347*, 45–51. https://doi.org/10.1111/nyas.12726.
41. Klos, K.S., Wyszomierski, S.L., Sun, M., Tan, M., Zhou, X., Li, P., Yang, W., Yin, G., Hittelman, W.N., and Yu, D. (2006). ErbB2 increases vascular endothelial growth factor protein synthesis via activation of mammalian target of rapamycin/p70S6K leading to increased angiogenesis and spontaneous metastasis of human breast cancer cells. Cancer Res. *66*, 2028–2037. https://doi.org/10.1158/0008-5472.CAN-04-4559.
42. Thorin, E., Labbé, P., Lambert, M., Mury, P., Dagher, O., Miquel, G., and Thorin-Trescases, N. (2023). Angiopoietin-Like Proteins: Cardiovascular Biology and Therapeutic Targeting for the Prevention of Cardiovascular Diseases. Can. J. Cardiol. *39*, 1736–1756. https://doi.org/10.1016/j.cjca.2023.06.002.
43. Lynch, C.N., Wang, Y.C., Lund, J.K., Chen, Y.W., Leal, J.A., and Wiley, S. R. (1999). TWEAK induces angiogenesis and proliferation of endothelial cells. J. Biol. Chem. *274*, 8455–8459. https://doi.org/10.1074/jbc.274.13.8455.
44. Lanier, V., Gillespie, C., Leffers, M., Daley-Brown, D., Milner, J., Lipsey, C., Webb, N., Anderson, L.M., Newman, G., Waltenberger, J., et al. (2016). Leptin-induced transphosphorylation of vascular endothelial growth factor receptor increases Notch and stimulates endothelial cell angiogenic transformation. Int. J. Biochem. Cell Biol. *79*, 139–150. https://doi.org/10.1016/j.biocel.2016.08.023.
45. Brouillet, S., Hoffmann, P., Benharouga, M., Salomon, A., Schaal, J.P., Feige, J.J., and Alfaidy, N. (2010). Molecular characterization of EG-VEGF-mediated angiogenesis: differential effects on microvascular and macrovascular endothelial cells. Mol. Biol. Cell *21*, 2832–2843. https://doi.org/10.1091/mbc.E10-01-0059.
46. Lawson, N.D., Vogel, A.M., and Weinstein, B.M. (2002). sonic hedgehog and vascular endothelial growth factor act upstream of the Notch pathway during arterial endothelial differentiation. Dev. Cell *3*, 127–136. https://doi.org/10.1016/s1534-5807(02)00198-3.
47. Lee, J., Goeckel, M.E., Levitas, A., Colijn, S., Shin, J., Hindes, A., Mun, G., Burton, Z., Chintalapati, B., Yin, Y., et al. (2024). CXCR3-CXCL11 Signaling Restricts Angiogenesis and Promotes Pericyte Recruitment. Arterioscler. Thromb. Vasc. Biol. *44*, 2577–2595. https://doi.org/10.1161/ATVBAHA.124.321434.
48. Frangogiannis, N.G. (2004). Chemokines in the ischemic myocardium: from inflammation to fibrosis. Inflamm. Res. *53*, 585–595. https://doi.org/10.1007/s00011-004-1298-5.
49. Ozhan, G., and Weidinger, G. (2015). Wnt/beta-catenin signaling in heart regeneration. Cell Regen. *4*, 3. https://doi.org/10.1186/s13619-015-0017-8.
50. Bayer, A.L., and Alcaide, P. (2021). MyD88: At the heart of inflammatory signaling and cardiovascular disease. J. Mol. Cell. Cardiol. *161*, 75–85. https://doi.org/10.1016/j.yjmcc.2021.08.001.
51. Feng, Y., Ye, D., Wang, Z., Pan, H., Lu, X., Wang, M., Xu, Y., Yu, J., Zhang, J., Zhao, M., et al. (2022). The Role of Interleukin-6 Family Members in Cardiovascular Diseases. Front. Cardiovasc. Med. *9*, 818890. https://doi.org/10.3389/fcvm.2022.818890.
52. Arenas-Ramirez, N., Woytschak, J., and Boyman, O. (2015). Interleukin-2: Biology, Design and Application. Trends Immunol. *36*, 763–777. https://doi.org/10.1016/j.it.2015.10.003.
53. Ishii, N., Takahashi, T., Soroosh, P., and Sugamura, K. (2010). OX40-OX40 ligand interaction in T-cell-mediated immunity and immunopathology. Adv. Immunol. *105*, 63–98. https://doi.org/10.1016/S0065-2776(10)05003-0.
54. Smith, C., Damås, J.K., Otterdal, K., Øie, E., Sandberg, W.J., Yndestad, A., Waehre, T., Scholz, H., Endresen, K., Olofsson, P.S., et al. (2006). Increased levels of neutrophil-activating peptide-2 in acute coronary syndromes: possible role of platelet-mediated vascular inflammation. J. Am. Coll. Cardiol. *48*, 1591–1599. https://doi.org/10.1016/j.jacc.2006.06.060.
55. O'Connell, P.A., Surette, A.P., Liwski, R.S., Svenningsson, P., and Waisman, D.M. (2010). S100A10 regulates plasminogen-dependent macrophage invasion. Blood *116*, 1136–1146. https://doi.org/10.1182/blood-2010-01-264754.

56. Cai, Y., Tan, W., Shen, X., Zhu, Y., Gao, Y., Sui, A., Lu, Q., Zhong, Y., and Xie, B. (2016). Neutralization of IL-23 depresses experimental ocular neovascularization. Exp. Eye Res. *146*, 242–251. https://doi.org/10.1016/j.exer.2016.02.008.

57. Brizzi, M.F., Garbarino, G., Rossi, P.R., Pagliardi, G.L., Arduino, C., Avanzi, G.C., and Pegoraro, L. (1993). Interleukin 3 stimulates proliferation and triggers endothelial-leukocyte adhesion molecule 1 gene activation of human endothelial cells. J. Clin. Invest. *91*, 2887–2892. https://doi.org/10.1172/JCI116534.

58. Kabashima, K., and Irie, H. (2021). Interleukin-31 as a Clinical Target for Pruritus Treatment. Front. Med. (Lausanne) *8*, 638325. https://doi.org/10.3389/fmed.2021.638325.

59. Ross, S.H., and Cantrell, D.A. (2018). Signaling and Function of Interleukin-2 in T Lymphocytes. Annu. Rev. Immunol. *36*, 411–433. https://doi.org/10.1146/annurev-immunol-042617-053352.

60. McGrath, E.E., Marriott, H.M., Lawrie, A., Francis, S.E., Sabroe, I., Renshaw, S.A., Dockrell, D.H., and Whyte, M.K.B. (2011). TNF-related apoptosis-inducing ligand (TRAIL) regulates inflammatory neutrophil apoptosis and enhances resolution of inflammation. J. Leukoc. Biol. *90*, 855–865. https://doi.org/10.1189/jlb.0211062.

61. NCBI (2024). TNFRSF12A TNF receptor superfamily member 12A [Homo sapiens (human)] (National Library of Medicine). https://www.ncbi.nlm.nih.gov/gene?Db=gene&Cmd=DetailsSearch&Term=51330.

62. Balan, S., Radford, K.J., and Bhardwaj, N. (2020). Unexplored horizons of cDC1 in immunity and tolerance. Adv. Immunol. *148*, 49–91. https://doi.org/10.1016/bs.ai.2020.10.002.

63. Brown, A.J., Sepuru, K.M., Sawant, K.V., and Rajarathnam, K. (2017). Platelet-Derived Chemokine CXCL7 Dimer Preferentially Exists in the Glycosaminoglycan-Bound Form: Implications for Neutrophil-Platelet Crosstalk. Front. Immunol. *8*, 1248. https://doi.org/10.3389/fimmu.2017.01248.

64. Okura, G.C., Bharadwaj, A.G., and Waisman, D.M. (2023). Recent Advances in Molecular and Cellular Functions of S100A10. Biomolecules *13*, 1450. https://doi.org/10.3390/biom13101450.

65. Chen, J.H., Wang, L.L., Tao, L., Qi, B., Wang, Y., Guo, Y.J., and Miao, L. (2021). Identification of MYH6 as the potential gene for human ischaemic cardiomyopathy. J. Cell. Mol. Med. *25*, 10736–10746. https://doi.org/10.1111/jcmm.17015.

66. Bischof, C., Mirtschink, P., Yuan, T., Wu, M., Zhu, C., Kaur, J., Pham, M.D., Gonzalez-Gonoggia, S., Hammer, M., Rogg, E.M., et al. (2021). Mitochondrial-cell cycle cross-talk drives endoreplication in heart disease. Sci. Transl. Med. *13*, eabi7964. https://doi.org/10.1126/scitranslmed.abi7964.

67. Zhao, Y., Wang, E.Y., Davenport, L.H., Liao, Y., Yeager, K., Vunjak-Novakovic, G., Radisic, M., and Zhang, B. (2019). A Multimaterial Microphysiological Platform Enabled by Rapid Casting of Elastic Microwires. Adv. Healthc. Mater. *8*, e1801187. https://doi.org/10.1002/adhm.201801187.

68. Nunes, S.S., Feric, N., Pahnke, A., Miklas, J.W., Li, M., Coles, J., Gagliardi, M., Keller, G., and Radisic, M. (2017). Human Stem Cell-Derived Cardiac Model of Chronic Drug Exposure. ACS Biomater. Sci. Eng. *3*, 1911–1921. https://doi.org/10.1021/acsbiomaterials.5b00496.

69. Boudou, T., Legant, W.R., Mu, A., Borochin, M.A., Thavandiran, N., Radisic, M., Zandstra, P.W., Epstein, J.A., Margulies, K.B., and Chen, C.S. (2012). A microfabricated platform to measure and manipulate the mechanics of engineered cardiac microtissues. Tissue Eng. Part A *18*, 910–919. https://doi.org/10.1089/ten.TEA.2011.0341.

70. Jackman, C.P., Carlson, A.L., and Bursac, N. (2016). Dynamic culture yields engineered myocardium with near-adult functional output. Biomaterials *111*, 66–79. https://doi.org/10.1016/j.biomaterials.2016.09.024.

71. Turnbull, I.C., Karakikes, I., Serrao, G.W., Backeris, P., Lee, J.J., Xie, C., Senyei, G., Gordon, R.E., Li, R.A., Akar, F.G., et al. (2014). Advancing functional engineered cardiac tissues toward a preclinical model of human myocardium. FASEB J. *28*, 644–654. https://doi.org/10.1096/fj.13-228007.

72. Huebsch, N., Loskill, P., Deveshwar, N., Spencer, C.I., Judge, L.M., Mandegar, M.A., Fox, C.B., Mohamed, T.M.A., Ma, Z., Mathur, A., et al. (2016). Miniaturized iPS-cell-derived cardiac muscles for physiologically relevant drug response analyses. Sci. Rep. *6*, 24726. https://doi.org/10.1038/srep24726.

73. Nunes, S.S., Miklas, J.W., Liu, J., Aschar-Sobbi, R., Xiao, Y., Zhang, B., Jiang, J., Massé, S., Gagliardi, M., Hsieh, A., et al. (2013). Biowire: a platform for maturation of human pluripotent stem cell–derived cardiomyocytes. Nat. Methods *10*, 781–787. https://doi.org/10.1038/nmeth.2524. https://www.nature.com/articles/nmeth.2524#supplementary-information.

74. Jain, R.K., Au, P., Tam, J., Duda, D.G., and Fukumura, D. (2005). Engineering vascularized tissue. Nat. Biotechnol. *23*, 821–823. https://doi.org/10.1038/nbt0705-821.

75. Thavandiran, N., Dubois, N., Mikryukov, A., Massé, S., Beca, B., Simmons, C.A., Deshpande, V.S., McGarry, J.P., Chen, C.S., Nanthakumar, K., et al. (2013). Design and formulation of functional pluripotent stem cell-derived cardiac microtissues. Proc. Natl. Acad. Sci. USA *110*, E4698–E4707. https://doi.org/10.1073/pnas.1311120110.

76. Ronaldson-Bouchard, K., Ma, S.P., Yeager, K., Chen, T., Song, L., Sirabella, D., Morikawa, K., Teles, D., Yazawa, M., and Vunjak-Novakovic, G. (2018). Advanced maturation of human cardiac tissue grown from pluripotent stem cells. Nature *556*, 239–243. https://doi.org/10.1038/s41586-018-0016-3.

77. Mannhardt, I., Breckwoldt, K., Letuffe-Brenière, D., Schaaf, S., Schulz, H., Neuber, C., Benzin, A., Werner, T., Eder, A., Schulze, T., et al. (2016). Human Engineered Heart Tissue: Analysis of Contractile Force. Stem Cell Rep. *7*, 29–42. https://doi.org/10.1016/j.stemcr.2016.04.011.

78. Ahrens, J.H., Uzel, S.G.M., Skylar-Scott, M., Mata, M.M., Lu, A., Kroll, K.T., and Lewis, J.A. (2022). Programming Cellular Alignment in Engineered Cardiac Tissue via Bioprinting Anisotropic Organ Building Blocks. Adv. Mater. *34*, e2200217. https://doi.org/10.1002/adma.202200217.

79. Kobayashi, H., Tohyama, S., Ichimura, H., Ohashi, N., Chino, S., Soma, Y., Tani, H., Tanaka, Y., Yang, X., Shiba, N., et al. (2024). Regeneration of Nonhuman Primate Hearts With Human Induced Pluripotent Stem Cell-Derived Cardiac Spheroids. Circulation *150*, 611–621. https://doi.org/10.1161/CIRCULATIONAHA.123.064876.

80. Kawaguchi, S., Soma, Y., Nakajima, K., Kanazawa, H., Tohyama, S., Tabei, R., Hirano, A., Handa, N., Yamada, Y., Okuda, S., et al. (2021). Intramyocardial Transplantation of Human iPS Cell-Derived Cardiac Spheroids Improves Cardiac Function in Heart Failure Animals. JACC Basic Transl. Sci. *6*, 239–254. https://doi.org/10.1016/j.jacbts.2020.11.017.

81. Tabei, R., Kawaguchi, S., Kanazawa, H., Tohyama, S., Hirano, A., Handa, N., Hishikawa, S., Teratani, T., Kunita, S., Fukuda, J., et al. (2019). Development of a transplant injection device for optimal distribution and retention of human induced pluripotent stem cell−derived cardiomyocytes. J. Heart Lung Transplant. *38*, 203–214. https://doi.org/10.1016/j.healun.2018.11.002.

82. National Library of Medicine. (2024). A Study of iPS Cell-derived Cardiomyocyte Spheroids (HS-001) in Patients With Heart Failure (LAPiS Study) (LAPiS). ClinicalTrials.org.

83. Rajasekar, S., Lin, D.S.Y., Abdul, L., Liu, A., Sotra, A., Zhang, F., and Zhang, B. (2020). IFlowPlate-A Customized 384-Well Plate for the Culture of Perfusable Vascularized Colon Organoids. Adv. Mater. *32*, e2002974. https://doi.org/10.1002/adma.202002974.

84. Kinnear, C., Said, A., Meng, G., Zhao, Y., Wang, E.Y., Rafatian, N., Parmar, N., Wei, W., Billia, F., Simmons, C.A., et al. (2024). Myosin inhibitor reverses hypertrophic cardiomyopathy in genotypically diverse pediatric iPSC-cardiomyocytes to mirror variant correction. Cell Rep. Med. *5*, 101520. https://doi.org/10.1016/j.xcrm.2024.101520.

85. Hamidzada, H., Pascual-Gil, S., Wu, Q., Kent, G.M., Massé, S., Kantores, C., Kuzmanov, U., Gomez-Garcia, M.J., Rafatian, N., Gorman, R.A., et al. (2024). Primitive macrophages induce sarcomeric maturation and

functional enhancement of developing human cardiac microtissues via efferocytic pathways. Nat CardioVasc Res *3*, 567–593. https://doi.org/10.1038/s44161-024-00471-7.

86. Cho, S., Dadson, K., Sung, H.K., Ayansola, O., Mirzaesmaeili, A., Noskovicova, N., Zhao, Y., Cheung, K., Radisic, M., Hinz, B., et al. (2024). Cardioprotection by the adiponectin receptor agonist ALY688 in a preclinical mouse model of heart failure with reduced ejection fraction (HFrEF). Biomed. Pharmacother. *171*, 116119. https://doi.org/10.1016/j.biopha.2023.116119.
87. Degli-Esposti, M.A., Dougall, W.C., Smolak, P.J., Waugh, J.Y., Smith, C.A., and Goodwin, R.G. (1997). The novel receptor TRAIL-R4 induces NF-kappaB and protects against TRAIL-mediated apoptosis, yet retains an incomplete death domain. Immunity *7*, 813–820. https://doi.org/10.1016/s1074-7613(00)80399-4.
88. Trebing, J., Arana, J.A.C., Salzmann, S., and Wajant, H. (2014). Analyzing the signaling capabilities of soluble and membrane TWEAK. Methods Mol. Biol. *1155*, 31–45. https://doi.org/10.1007/978-1-4939-0669-7_4.
89. Durda, P., Sabourin, J., Lange, E.M., Nalls, M.A., Mychaleckyj, J.C., Jenny, N.S., Li, J., Walston, J., Harris, T.B., Psaty, B.M., et al. (2015). Plasma Levels of Soluble Interleukin-2 Receptor α: Associations With Clinical Cardiovascular Events and Genome-Wide Association Scan. Arterioscler. Thromb. Vasc. Biol. *35*, 2246–2253. https://doi.org/10.1161/ATVBAHA.115.305289.
90. Akkenepally, S.V., Yombo, D.J.K., Yerubandi, S., Reddy, G.B., Deshpande, D.A., McCormack, F.X., and Madala, S.K. (2023). Interleukin 31 receptor alpha promotes smooth muscle cell contraction and airway hyperresponsiveness in asthma. Nat. Commun. *14*, 8207. https://doi.org/10.1038/s41467-023-44040-1.
91. Schwartzkopff, F., Brandt, E., Petersen, F., Flad, H.D., Bock, L., and Ludwig, A. (2002). The CXC chemokine NAP-2 mediates differential heterologous desensitization of neutrophil effector functions elicited by platelet-activating factor. J. Interferon Cytokine Res. *22*, 257–267. https://doi.org/10.1089/107999002753536239.
92. Nakano, M., Fukumoto, Y., Satoh, K., Ito, Y., Kagaya, Y., Ishii, N., Sugamura, K., and Shimokawa, H. (2010). OX40 ligand plays an important role in the development of atherosclerosis through vasa vasorum neovascularization. Cardiovasc. Res. *88*, 539–546. https://doi.org/10.1093/cvr/cvq211.
93. Welti, J., Loges, S., Dimmeler, S., and Carmeliet, P. (2013). Recent molecular discoveries in angiogenesis and antiangiogenic therapies in cancer. J. Clin. Invest. *123*, 3190–3200. https://doi.org/10.1172/JCI70212.
94. Strasser, G.A., Kaminker, J.S., and Tessier-Lavigne, M. (2010). Microarray analysis of retinal endothelial tip cells identifies CXCR4 as a mediator of tip cell morphology and branching. Blood *115*, 5102–5110. https://doi.org/10.1182/blood-2009-07-230284.
95. Fernández, C.A., and Moses, M.A. (2006). Modulation of angiogenesis by tissue inhibitor of metalloproteinase-4. Biochem. Biophys. Res. Commun. *345*, 523–529. https://doi.org/10.1016/j.bbrc.2006.04.083.
96. Eriksson, A., Cao, R., Pawliuk, R., Berg, S.M., Tsang, M., Zhou, D., Fleet, C., Tritsaris, K., Dissing, S., Leboulch, P., et al. (2002). Placenta growth factor-1 antagonizes VEGF-induced angiogenesis and tumor growth by the formation of functionally inactive PlGF-1/VEGF heterodimers. Cancer Cell *1*, 99–108. https://doi.org/10.1016/s1535-6108(02)00028-4.
97. Maisonpierre, P.C., Suri, C., Jones, P.F., Bartunkova, S., Wiegand, S.J., Radziejewski, C., Compton, D., McClain, J., Aldrich, T.H., Papadopoulos, N., et al. (1997). Angiopoietin-2, a natural antagonist for Tie2 that disrupts in vivo angiogenesis. Science *277*, 55–60. https://doi.org/10.1126/science.277.5322.55.
98. Guo, Y.L., Wang, S., and Colman, R.W. (2001). Kininostatin, an angiogenic inhibitor, inhibits proliferation and induces apoptosis of human endothelial cells. Arterioscler. Thromb. Vasc. Biol. *21*, 1427–1433. https://doi.org/10.1161/hq0901.095277.
99. Ueno, S., Weidinger, G., Osugi, T., Kohn, A.D., Golob, J.L., Pabon, L., Reinecke, H., Moon, R.T., and Murry, C.E. (2007). Biphasic role for Wnt/beta-catenin signaling in cardiac specification in zebrafish and embryonic stem cells. Proc. Natl. Acad. Sci. USA *104*, 9685–9690. https://doi.org/10.1073/pnas.0702859104.
100. Balatskyi, V.V., Sowka, A., Dobrzyn, P., and Piven, O.O. (2023). WNT/beta-catenin pathway is a key regulator of cardiac function and energetic metabolism. Acta Physiol. (Oxf.) *237*, e13912. https://doi.org/10.1111/apha.13912.
101. Gross, J.C., and Zelarayán, L.C. (2018). The Mingle-Mangle of Wnt Signaling and Extracellular Vesicles: Functional Implications for Heart Research. Front. Cardiovasc. Med. *5*, 10. https://doi.org/10.3389/fcvm.2018.00010.
102. Xia, J.B., Liu, G.H., Chen, Z.Y., Mao, C.Z., Zhou, D.C., Wu, H.Y., Park, K.S., Zhao, H., Kim, S.K., Cai, D.Q., et al. (2016). Hypoxia/ischemia promotes CXCL10 expression in cardiac microvascular endothelial cells by NFkB activation. Cytokine *81*, 63–70. https://doi.org/10.1016/j.cyto.2016.02.007.
103. Byappanahalli, A.M., Omoniyi, V., Noren Hooten, N., Smith, J.T., Mode, N.A., Ezike, N., Zonderman, A.B., and Evans, M.K. (2024). Extracellular vesicle mitochondrial DNA levels are associated with race and mitochondrial DNA haplogroup. iScience *27*, 108724. https://doi.org/10.1016/j.isci.2023.108724.
104. Wagner, K.T., Lu, R.X.Z., Landau, S., Shawky, S.A., Zhao, Y., Bodenstein, D.F., Jiménez Vargas, L.F., Jiang, R., Okhovatian, S., Wang, Y., et al. (2024). Endothelial extracellular vesicles enhance vascular self-assembly in engineered human cardiac tissues. Biofabrication *16*, 045037. https://doi.org/10.1088/1758-5090/ad76d9.
105. Dvir, T., Kedem, A., Ruvinov, E., Levy, O., Freeman, I., Landa, N., Holbova, R., Feinberg, M.S., Dror, S., Etzion, Y., et al. (2009). Prevascularization of cardiac patch on the omentum improves its therapeutic outcome. Proc. Natl. Acad. Sci. USA *106*, 14990–14995. https://doi.org/10.1073/pnas.0812242106.
106. Meza-Perez, S., and Randall, T.D. (2017). Immunological Functions of the Omentum. Trends Immunol. *38*, 526–536. https://doi.org/10.1016/j.it.2017.03.002.
107. Kawamura, M., Miyagawa, S., Fukushima, S., Saito, A., Miki, K., Ito, E., Sougawa, N., Kawamura, T., Daimon, T., Shimizu, T., et al. (2013). Enhanced survival of transplanted human induced pluripotent stem cell-derived cardiomyocytes by the combination of cell sheets with the pedicled omental flap technique in a porcine heart. Circulation *128*, S87–S94. https://doi.org/10.1161/CIRCULATIONAHA.112.000366.
108. Kawamura, M., Miyagawa, S., Fukushima, S., Saito, A., Miki, K., Funakoshi, S., Yoshida, Y., Yamanaka, S., Shimizu, T., Okano, T., et al. (2017). Enhanced Therapeutic Effects of Human iPS Cell Derived-Cardiomyocyte by Combined Cell-Sheets with Omental Flap Technique in Porcine Ischemic Cardiomyopathy Model. Sci. Rep. *7*, 8824. https://doi.org/10.1038/s41598-017-08869-z.
109. Wang, H., Roche, C.D., and Gentile, C. (2020). Omentum support for cardiac regeneration in ischaemic cardiomyopathy models: a systematic scoping review. Eur. J. Cardiothorac. Surg. *58*, 1118–1129. https://doi.org/10.1093/ejcts/ezaa205.
110. Tanaka, Y., Kadota, S., Zhao, J., Kobayashi, H., Okano, S., Izumi, M., Honda, Y., Ichimura, H., Shiba, N., Uemura, T., et al. (2023). Mature human induced pluripotent stem cell-derived cardiomyocytes promote angiogenesis through alpha-B crystallin. Stem Cell Res. Ther. *14*, 240. https://doi.org/10.1186/s13287-023-03468-4.
111. Lv, Y., Kim, K., Sheng, Y., Cho, J., Qian, Z., Zhao, Y.Y., Hu, G., Pan, D., Malik, A.B., and Hu, G. (2018). YAP Controls Endothelial Activation and Vascular Inflammation Through TRAF6. Circ. Res. *123*, 43–56. https://doi.org/10.1161/CIRCRESAHA.118.313143.
112. Mia, M.M., Cibi, D.M., Ghani, S.A.B.A., Singh, A., Tee, N., Sivakumar, V., Bogireddi, H., Cook, S.A., Mao, J., and Singh, M.K. (2022). Loss of Yap/Taz in cardiac fibroblasts attenuates adverse remodelling and improves cardiac function. Cardiovasc. Res. *118*, 1785–1804. https://doi.org/10.1093/cvr/cvab205.

113. Lin, Z., von Gise, A., Zhou, P., Gu, F., Ma, Q., Jiang, J., Yau, A.L., Buck, J. N., Gouin, K.A., van Gorp, P.R.R., et al. (2014). Cardiac-specific YAP activation improves cardiac function and survival in an experimental murine MI model. Circ. Res. *115*, 354–363. https://doi.org/10.1161/CIRCRESAHA.115.303632.

114. Ou, W.B., Lundberg, M.Z., Zhu, S., Bahri, N., Kyriazoglou, A., Xu, L., Chen, T., Mariño-Enriquez, A., and Fletcher, J.A. (2021). YWHAE-NUTM2 oncoprotein regulates proliferation and cyclin D1 via RAF/MAPK and Hippo pathways. Oncogenesis *10*, 37. https://doi.org/10.1038/s41389-021-00327-w.

115. Jebran, A.F., Seidler, T., Tiburcy, M., Daskalaki, M., Kutschka, I., Fujita, B., Ensminger, S., Bremmer, F., Moussavi, A., Yang, H., et al. (2025). Engineered heart muscle allografts for heart repair in primates and humans. Nature *639*, 503–511. https://doi.org/10.1038/s41586-024-08463-0.

116. Cai, L., Dewi, R.E., and Heilshorn, S.C. (2015). Injectable Hydrogels with In Situ Double Network Formation Enhance Retention of Transplanted Stem Cells. Adv. Funct. Mater. *25*, 1344–1351. https://doi.org/10.1002/adfm.201403631.

117. Perez-Riverol, Y., Csordas, A., Bai, J., Bernal-Llinares, M., Hewapathirana, S., Kundu, D.J., Inuganti, A., Griss, J., Mayer, G., Eisenacher, M., et al. (2019). The PRIDE database and related tools and resources in 2019: improving support for quantification data. Nucleic Acids Res. *47*, D442–D450. https://doi.org/10.1093/nar/gky1106.

118. Landau, S., Shor, E., Radisic, M., and Levenberg, S. (2024). Quantitative Image Analysis of Tissue Properties: A MATLAB Tool for Measuring Morphology and Co-localization in 2D Images. Preprint at bioRxiv.

119. Tyanova, S., Temu, T., Sinitcyn, P., Carlson, A., Hein, M.Y., Geiger, T., Mann, M., and Cox, J. (2016). The Perseus computational platform for comprehensive analysis of (prote)omics data. Nat. Methods *13*, 731–740. https://doi.org/10.1038/nmeth.3901.

120. Doncheva, N.T., Morris, J.H., Gorodkin, J., and Jensen, L.J. (2019). Cytoscape StringApp: network analysis and visualization of proteomics data. J. Proteome Res. *18*, 623–632. https://doi.org/10.1021/acs.jproteome.8b00702.